Supporting Information for "A new P-wave Tomographic Model (CAP22) for North America: Implications for the Subduction and Cratonic Metasomatic Modification History of Western Canada and Alaska"

A. Boyce[1*], M. V. Liddell[2], S. Pugh[1], J. Brown[1], E. McMurchie[1], A. Parsons[1], C. Estève[3], S. Burdick[4], F. A. Darbyshire[2], S. Cottaar[1], I. D. Bastow[5], A. J. Schaeffer[6], P. Audet[7], D. L. Schutt[8], R. C. Aster[8]

[1]University of Cambridge, Department of Earth Science, Bullard Laboratories, Madingley Road, Cambridge, CB3 0EZ, UK.

[2]Centre de recherche Geotop, Université du Québec à Montréal, QC, Canada

[3]Department of Meteorology and Geophysics, University of Vienna, Vienna, Austria

[4]Wayne State University, Geology Department, Detroit, MI, USA

[5]Department of Earth Science and Engineering, Royal School of Mines, Prince Consort Road, Imperial College London, London, SW7 2BP, UK.

[6]Geological Survey of Canada Pacific Division, Sidney, BC, Canada

[7]University of Ottawa, Department of Earth and Environmental Sciences, Ottawa, ON, Canada

[8]Colorado State University, Department of Geosciences and Warner College of Natural Resources, Fort Collins, CO, USA

[*]Present Address: Université Lyon 1, ENS de Lyon, CNRS, UMR 5276 LGL-TPE, F-69622, Villeurbanne, France.

Corresponding author: Alistair Boyce, `alistair.boyce@univ-lyon1.fr`

Contents of this file

Introduction

A digital model file of the CAP22 tomographic model with and without the crustal correction is available at IRIS EMC (https://ds.iris.edu/ds/products/emc-cap22/ under the doi: 10.17611/dp/emc.2023.cap22.1). Below we give details of the data set, tomographic inversion and additional checkerboard tests.

The Global Data Set

Figures S1 and S2 show the earthquake and station locations used in the tomographic inversion. Phase arrivals from the EHB Bulletin are available at http://www.isc.ac.uk/ehbbulletin/. Phase arrivals from USArray are available to the community as CSS monthly files from the ANF (http://anf.ucsd.edu/tools/events/). We make use of further phase arrivals updated after Burdick et al. (2017), Boyce et al. (2019) and Boyce et al. (2021) to more accurately constrain the background model.

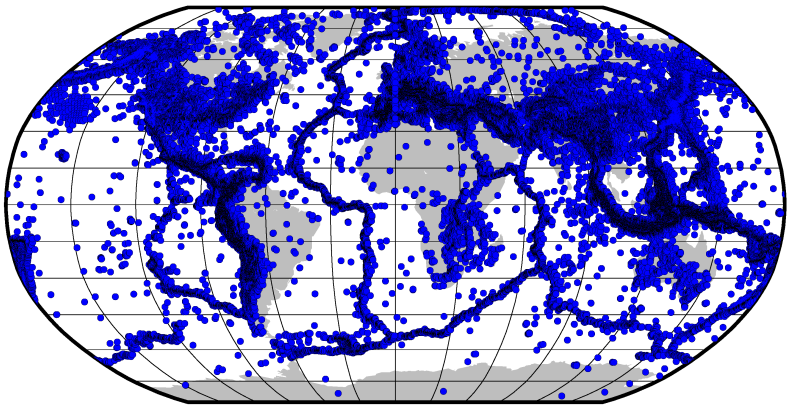

Figure S1. Earthquake map derived from the EHB Bulletin (see Li et al., 2008) and supplementary data updated after Burdick et al. (2017), Boyce et al. (2019) and Boyce et al. (2021), combined with newly incorporated teleseismic earthquakes recorded across North America.

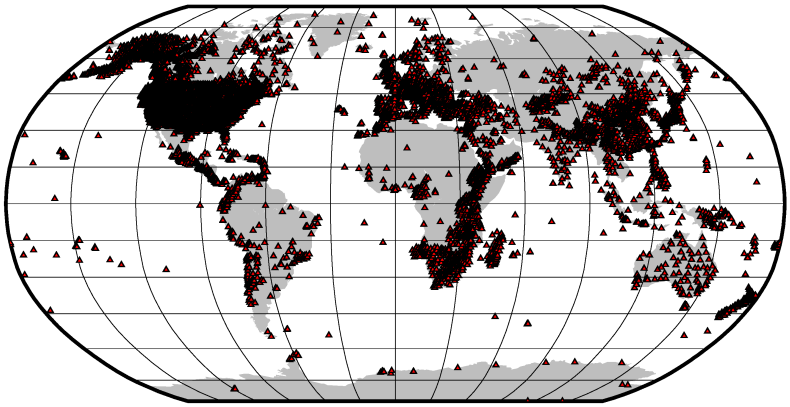

Figure S2. Seismograph station map derived from the EHB Bulletin (see Li et al., 2008) and supplementary data updated after Burdick et al. (2017), Boyce et al. (2019) and Boyce et al. (2021), combined with newly incorporated publicly available networks across North America.

Direct P-wave Absolute Arrival-time Residuals

Figure S3 shows the direct-P phase mean absolute arrival-time residuals for stations in the EHB database (Engdahl et al., 1998) used by Li et al. (2008), USArray stations and those from other temporary North American seismograph stations added here (see main manuscript). Residuals from other phases (e.g., Pn, Pg, pP, PKP and PKIKP) are not plotted but are used to better constrain the crust and deep mantle.

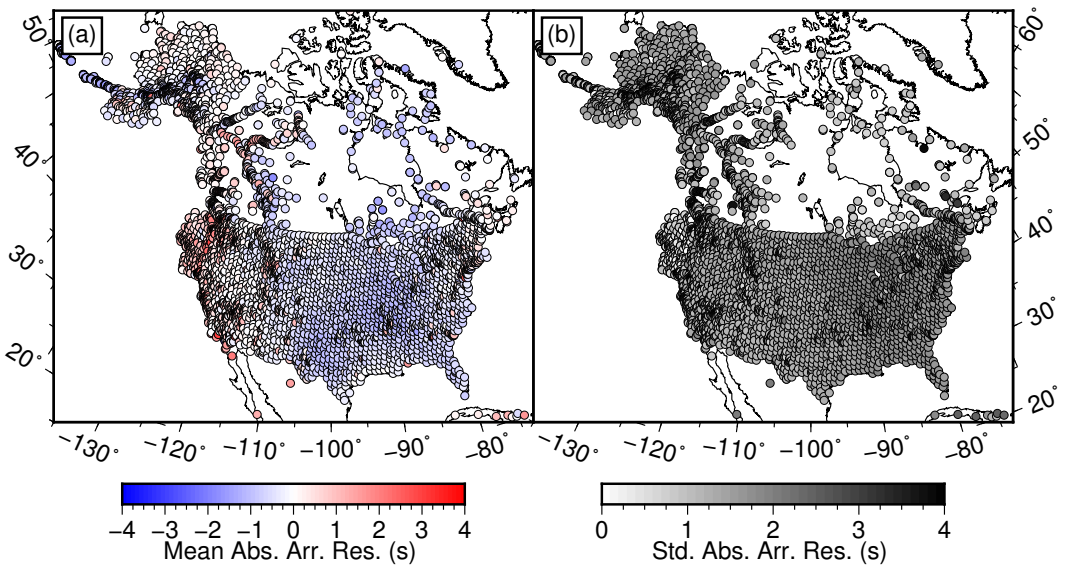

Figure S3. Mean *(a)* and standard deviation *(b)* of the direct-P phase absolute arrival-time residuals for the EHB database (Engdahl et al., 1998) used by Li et al. (2008), USArray stations and those from other North American data sets summarized in the main manuscript (Figure 2). Our newly added direct P-wave arrival-times from North American temporary seismograph stations total 202,719 absolute time picks. Residuals have been corrected for both station elevation and Earth's ellipticity.

Relative Arrival-time Analysis

We downloaded vertical component broadband seismic data from publicly available seismograph networks across Canada and Alaska over the period 2005–2020. We exclude data for the USArray Transportable Array as this is available in processed form already. We also exclude stations associated with glacial monitoring. We divide the station networks into seven subregions (Figure S4); Alaska OBS (ALO), Alaska land-stations (ALS), Alaska volcano network (ALV), Hudson Bay (HSB), Northwest Canada (NWC), Southwest Canada (SWC), Western US - Cascadia - OBS (WUO). For each subregion we obtain relative arrival-times separately using Multi-Channel Cross-correlation (VanDecar & Crosson, 1990) as outlined more precisely by Boyce et al. (2016). For NWC we reprocess the data from Estève et al. (2020) spanning 2002–2018 but exclude the USArray TA data. For HSB, we take directly the relative arrival-times calculated by Liddell et al. (2018) spanning 2004–2015 (replotted in Figure S8 and convert these to absolute-times in the following section.

For the Alaskan OBS data set 2,177 picks are derived from 98 earthquakes recorded at 89 stations recording data from 2018–2019. For the Alaskan land-station data set 96,110 picks are derived from 2,793 earthquakes recorded at 376 stations. For the Alaskan volcano network (ALV) data set 1,816 picks are derived from 37 earthquakes recorded at 127 stations. For the Hudson Bay data set 8,252 picks are derived from 668 earthquakes recorded at 62 stations. For the Northwest Canadian data set 39,507 picks are derived from 2,250 earthquakes recorded at 171 stations. For the Southwest Canadian data set 49,273 picks are derived from 2,276 earthquakes recorded at 302 stations. For the Western US - Cascadia - OBS data set 1,218 picks are derived from 69 earthquakes recorded at 256 stations recording data from 2010–2015. Figures S5–S11 document these results.

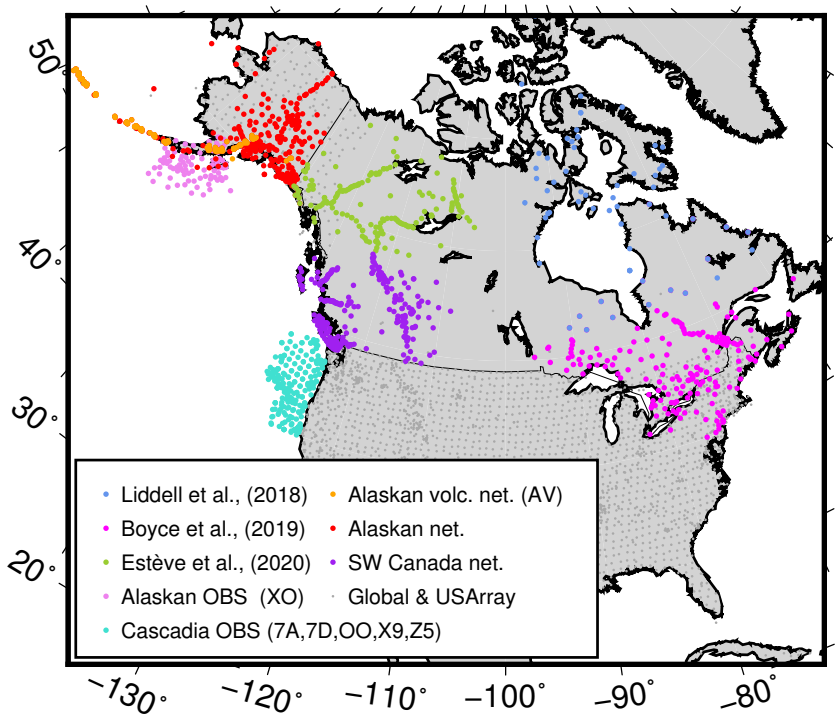

Figure S4. Map of publicly available seismic networks (colored) across Canada and Alaska, initially processed separately (Figures S5–S11), overlain on global and USArray TA network coverage (grey). Details of seismic networks used are found in the Open Research Section of the main manuscript.

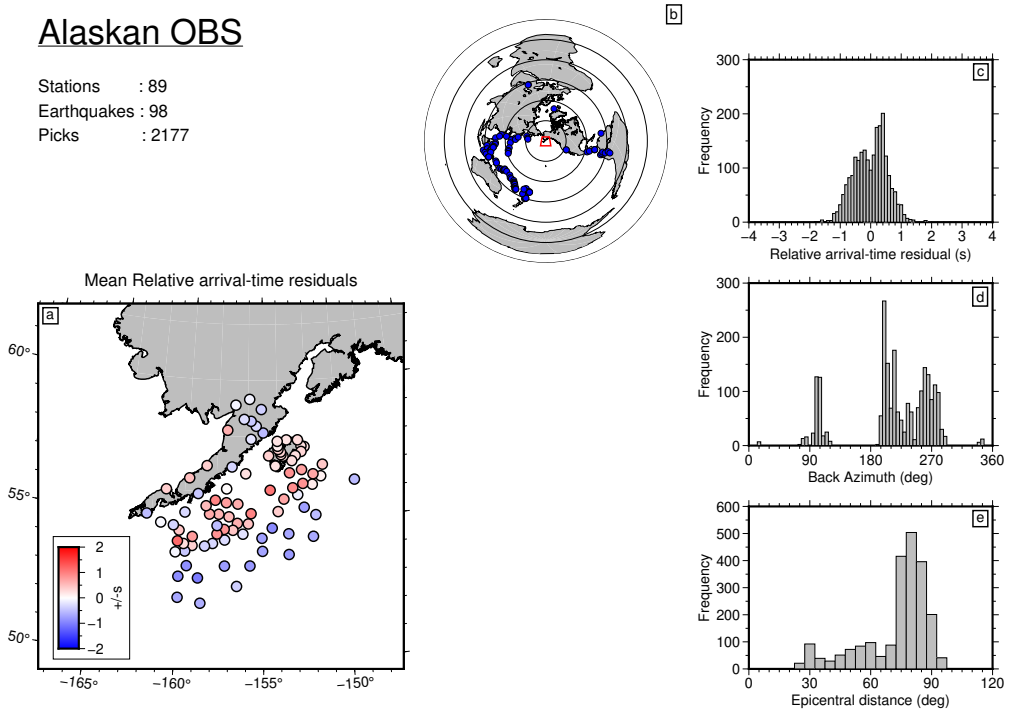

Figure S5. For the Alaskan OBS data set: (a) Map of station mean relative arrival-time residuals obtained using Multi-channel cross-correlation (VanDecar & Crosson, 1990). (b) Teleseismic earthquakes of magnitude $m_b \geq 6.0$ (blue dots) have adequate SNR at ≥ 4 stations across the regional network. Concentric rings are separated by 30° increments in epicentral distance from the center of the network. (c) Distribution of relative arrival-time residuals. (d) Residual distribution with back-azimuth. (e) Residual distribution with epicentral distance. Data sources: XO-2018 (Abers et al., 2018; Barcheck et al., 2020).

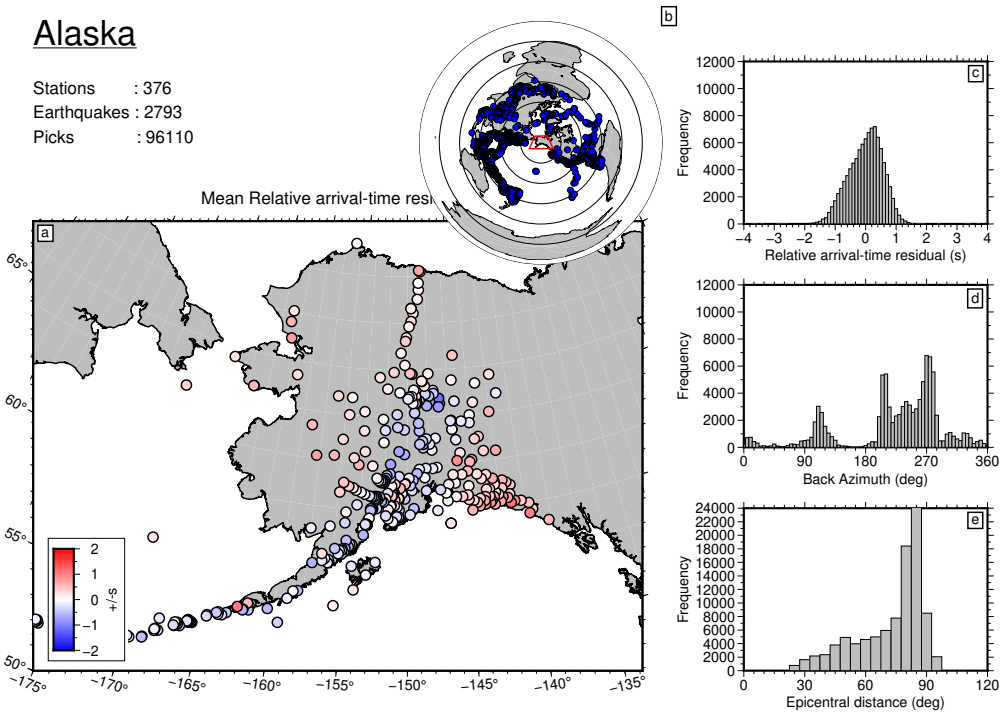

Figure S6. For the Alaskan land-station data set: (a) Map of station mean relative arrival-time residuals obtained using Multi-channel cross-correlation (VanDecar & Crosson, 1990). (b) Teleseismic earthquakes of magnitude $m_b \geq 5.5$ (blue dots) have adequate SNR at ≥ 4 stations across the regional network. Concentric rings are separated by 30° increments in epicentral distance from the center of the network. (c) Distribution of relative arrival-time residuals. (d) Residual distribution with back-azimuth. (e) Residual distribution with epicentral distance. Data sources: AK-1987 (Alaska Earthquake Center, Univ. of Alaska Fairbanks, 1987; D'Alessandro & Ruppert, 2012), AT-1967 (NOAA National Oceanic and Atmospheric Administration (USA), 1967; Oppenheimer et al., 2005), AV-1988 (Alaska Volcano Observatory/USGS, 1988; Dixon et al., 2013), GM-2016 (U.S. Geological Survey, 2016; Ringler et al., 2021), II-1986 (Scripps Institution of Oceanography, 1986; Ringler et al., 2021), IM-1965 (Various Authors, 1965; Ringler et al., 2021), IU-2014 (Albuquerque Seismological Laboratory/USGS, 2014; Ringler et al., 2021), PN-1998 (Indiana University Bloomington (IU Bloomington), 1998), US-1990 (Albuquerque Seismological Laboratory (ASL)/USGS, 1990; Ringler et al., 2021), XM-2011 (Keranen, 2011), XR-2004 (Song & Christensen, 2004), XV-2007 (Larsen & Truffer, 2007), XZ-2005 (Hansen & Pavlis, 2005; Berger et al., 2008), ZE-2015 (Tape et al., 2015, 2017).

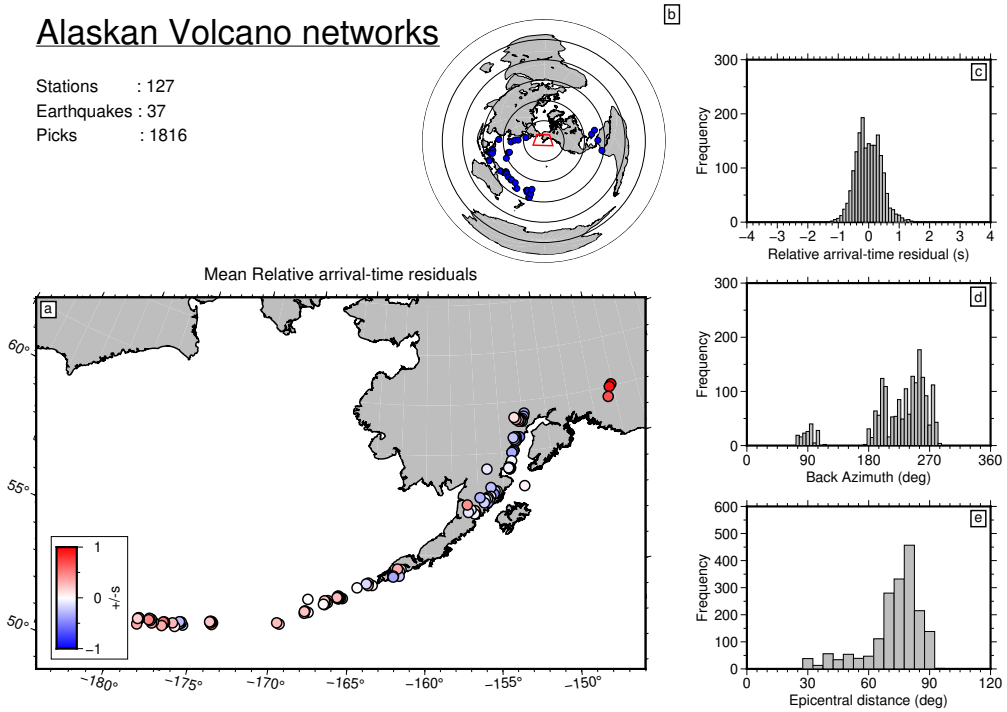

Figure S7. For the Alaskan volcano network (ALV) data set: (*a*) Map of station mean relative arrival-time residuals obtained using Multi-channel cross-correlation (VanDecar & Crosson, 1990). (*b*) Teleseismic earthquakes of magnitude $m_b \geq 5.5$ (blue dots) have adequate SNR at ≥ 4 stations across the regional network. Concentric rings are separated by 30° increments in epicentral distance from the center of the network. (*c*) Distribution of relative arrival-time residuals. (*d*) Residual distribution with back-azimuth. (*e*) Residual distribution with epicentral distance. Data sources: AV-1988 (Alaska Volcano Observatory/USGS, 1988; Dixon et al., 2013).

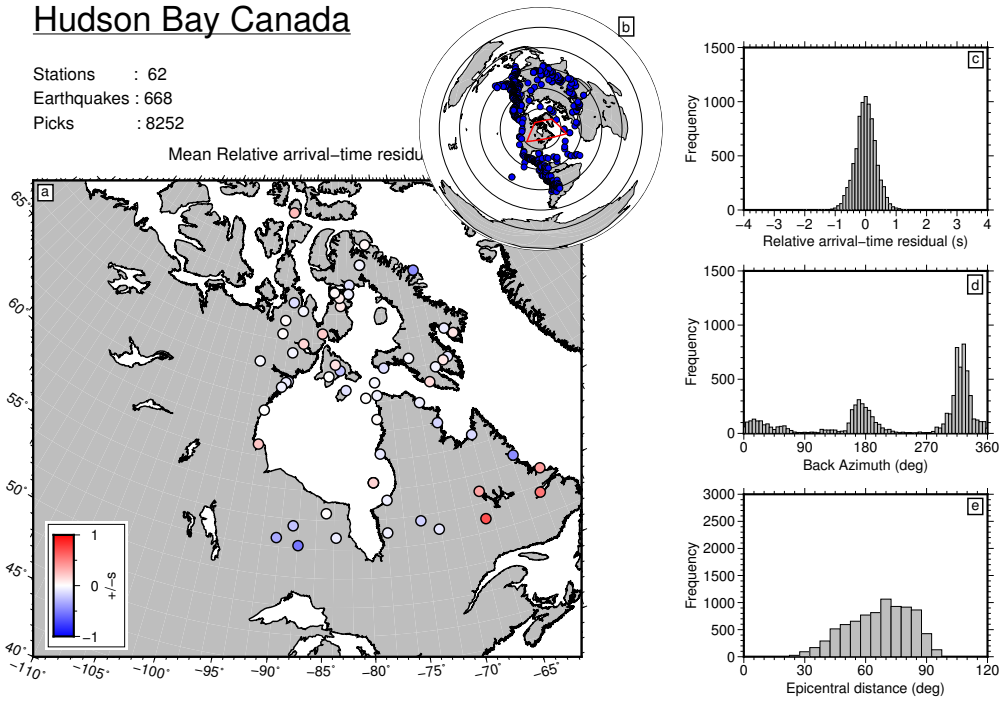

Figure S8. For the Hudson Bay data set: (a) Map of station mean relative arrival-time residuals. (b) Teleseismic earthquakes of magnitude $m_b \geq 5.5$ (blue dots) have adequate SNR at ≥ 4 stations across the regional network. Concentric rings are separated by 30° increments in epicentral distance from the center of the network. (c) Distribution of relative arrival-time residuals. (d) Residual distribution with back-azimuth. (e) Residual distribution with epicentral distance. Plot produced using the relative arrival-time data of (Liddell et al., 2018). Data sources: CN-1975 (Natural Resources Canada (NRCAN Canada), 1975; North, 1994; Bent et al., 2019), PO-2000 (Geological Survey of Canada, 2000; Eaton et al., 2004; Snyder et al., 2003), X5-2007 (University of Bristol (UK), 2007; Bastow et al., 2015).

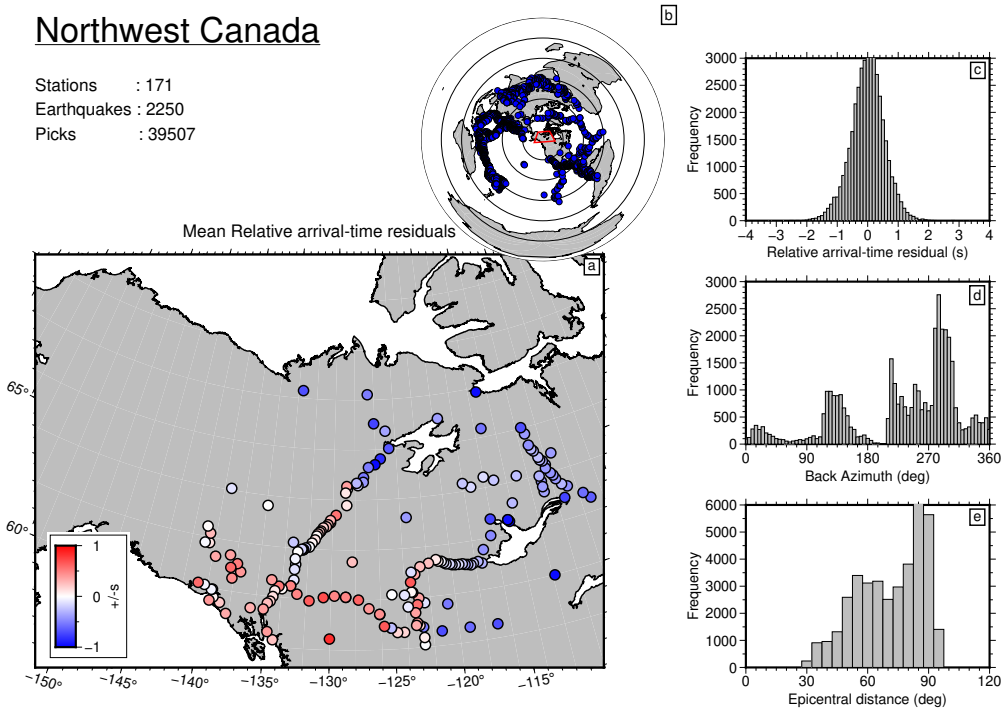

Figure S9. For the Northwest Canadian data set: (a) Map of station mean relative arrival-time residuals obtained using Multi-channel cross-correlation (VanDecar & Crosson, 1990), reprocessed after Estève et al. (2020). (b) Teleseismic earthquakes of magnitude $m_b \geq 6.0$ (blue dots) have adequate SNR at ≥ 4 stations across the regional network. Concentric rings are separated by 30° increments in epicentral distance from the center of the network. (c) Distribution of relative arrival-time residuals. (d) Residual distribution with back-azimuth. (e) Residual distribution with epicentral distance. Data sources: CN-1975 (Natural Resources Canada (NRCAN Canada), 1975; North, 1994; Bent et al., 2019), NY-2013 (University of Ottawa (uOttawa Canada), 2013; Estève et al., 2020), PO-2000 (Geological Survey of Canada, 2000; Eaton et al., 2004; Snyder et al., 2003), RV-2013 (Alberta Geological Survey / Alberta Energy Regulator, 2013; Schultz et al., 2015), XN-2003 (Gaherty & Revenaugh, 2003; Mercier et al., 2009), Y5-2006 (University of Alberta (UAlberta Canada), 2006; Gu et al., 2011), YO-2016 (Yukon Geological Survey, 206; Estève et al., 2019), 7C-2015 (Schutt & Aster, 2015; Baker et al., 2020).

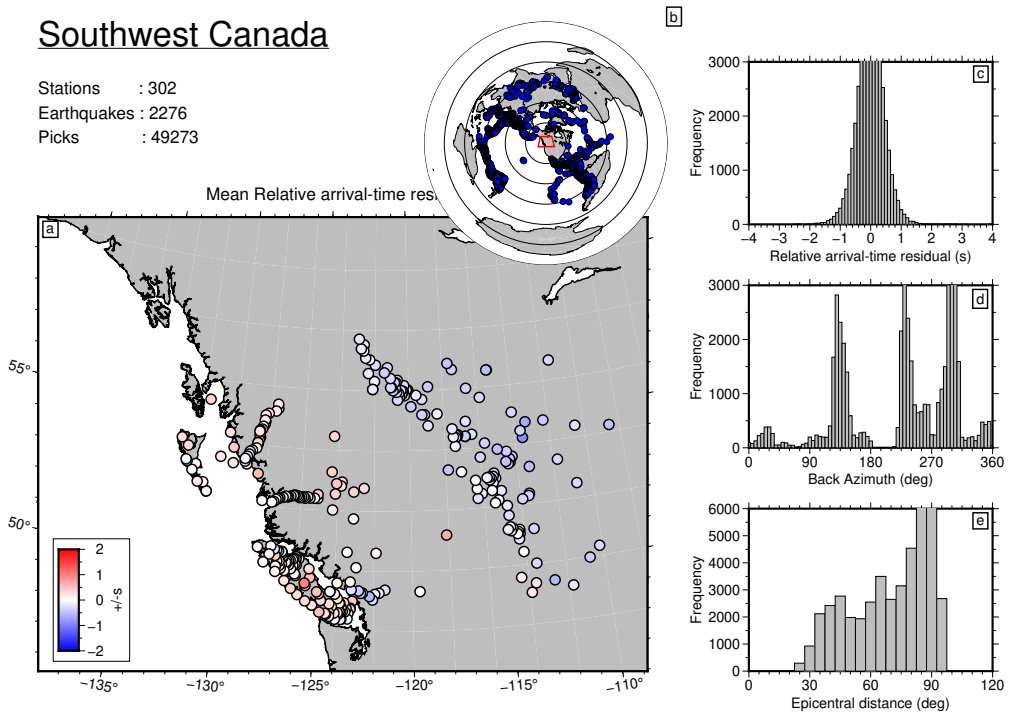

Figure S10. For the Southwest Canadian data set: (a) Map of station mean relative arrival-time residuals obtained using Multi-channel cross-correlation (VanDecar & Crosson, 1990). (b) Teleseismic earthquakes of magnitude $m_b \geq 5.5$ (blue dots) have adequate SNR at ≥ 4 stations across the regional network. Concentric rings are separated by 30° increments in epicentral distance from the center of the network. (c) Distribution of relative arrival-time residuals. (d) Residual distribution with back-azimuth. (e) Residual distribution with epicentral distance. Data sources: 1E-2018 (Natural Resources Canada (NRCAN Canada), 2018; Babaie Mahani et al., 2019), 2K-2014 (Schultz et al., 2014, 2020), AK-1987 (Alaska Earthquake Center, Univ. of Alaska Fairbanks, 1987; D'Alessandro & Ruppert, 2012), C8-2002 (Natural Resources Canada (NRCAN Canada), 2002), CN-1975 (Natural Resources Canada (NRCAN Canada), 1975; North, 1994; Bent et al., 2019), EO-2018 (University of Calgary (U of C Canada), 2018; Boggs et al., 2018), PO-2000 (Geological Survey of Canada, 2000; Eaton et al., 2004; Snyder et al., 2003), RV-2013 (Alberta Geological Survey / Alberta Energy Regulator, 2013; Schultz et al., 2015), TD-2013 (TransAlta Corporation, 2013; Cui & Atkinson, 2016), XL-2017 (McGill University (Canada), 2017; Roth et al., 2020), XN-2003 (Gaherty & Revenaugh, 2003; Mercier et al., 2009), XY-2005 (Dueker & Zandt, 2005; Calkins et al., 2010), Y5-2006 (University of Alberta (UAlberta Canada), 2006; Gu et al., 2011).

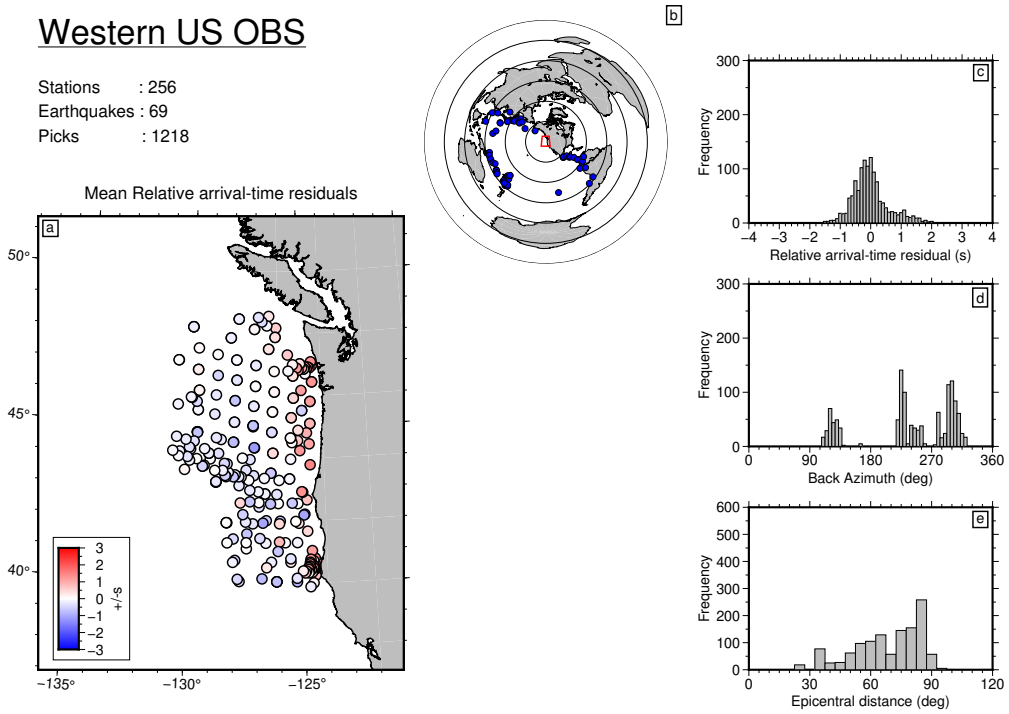

Figure S11. For the Western US (Cascadia) OBS data set: (*a*) Map of station mean relative arrival-time residuals obtained using Multi-channel cross-correlation (VanDecar & Crosson, 1990). (*b*) Teleseismic earthquakes of magnitude $m_b \geq 5.5$ (blue dots) have adequate SNR at ≥ 4 stations across the regional network. Concentric rings are separated by 30° increments in epicentral distance from the center of the network. (*c*) Distribution of relative arrival-time residuals. (*d*) Residual distribution with back-azimuth. (*e*) Residual distribution with epicentral distance. Data sources: (see Toomey et al., 2014): 7A-2010 (Woods Hole Oceanographic Institution (WHOI), 2010), 7D-2011 (IRIS OBSIP, 2011), OO-2013 (Rutgers University, 2013), X9-2012 (Nabelek & Braunmiller, 2012), Z5-2013 (Nabelek & Braunmiller, 2013)

Absolute Arrival-time Analysis

We next convert relative arrival-times derived from the subregions in the previous section to absolute arrival-times using the Absolute Arrival-time Recovery Method (AARM - see Boyce et al., 2017). Absolute arrival-time residuals are calculated with respect to the global mean and can therefore be combined with global pick databases. AARM yields 2,076 picks for the Alaskan OBS data set, 91,429 picks for the Alaskan land-station data set, 1,756 picks for the Alaskan volcano network (ALV) data set, 8,252 picks for the Hudson Bay data set, 37,444 picks for the Northwest Canadian data set, 44,270 picks for the Southwest Canadian data set and 1,095 picks for the Western US (Cascadia) OBS data set (Figures S12–S18).

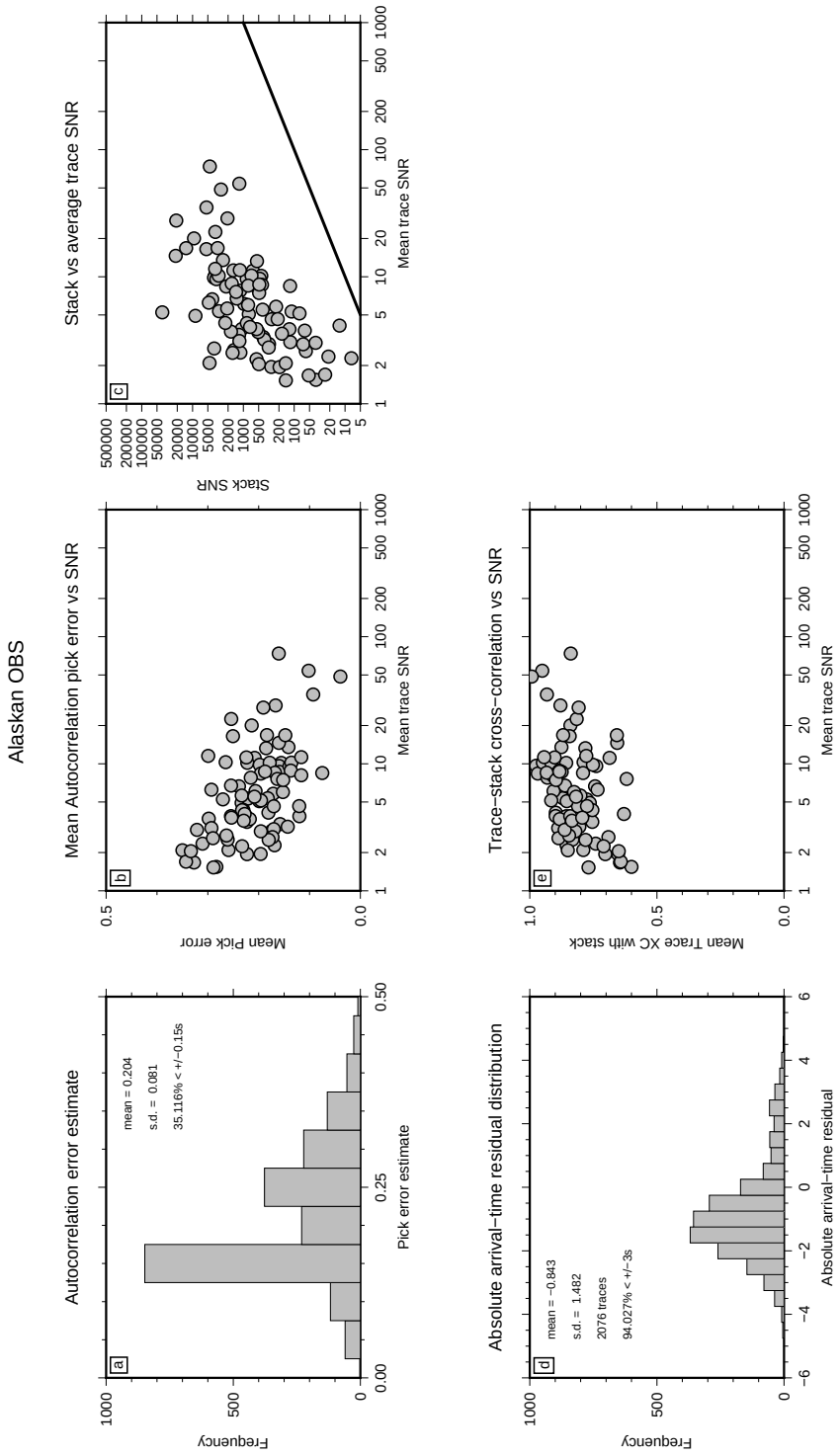

Figure S12. For the Alaskan OBS data set: (*a*) Distribution of autocorrelation pick error estimates for each arrival-time. (*b*) Mean autocorrelation pick error against mean trace SNR for each earthquake. (*c*) Stacked trace SNR against mean trace SNR for each earthquake. Line y=x (black line). (*d*) Distribution of absolute arrival-time residuals. (*e*) Mean cross-correlation coefficient of each trace with the stack against mean trace SNR for each earthquake.

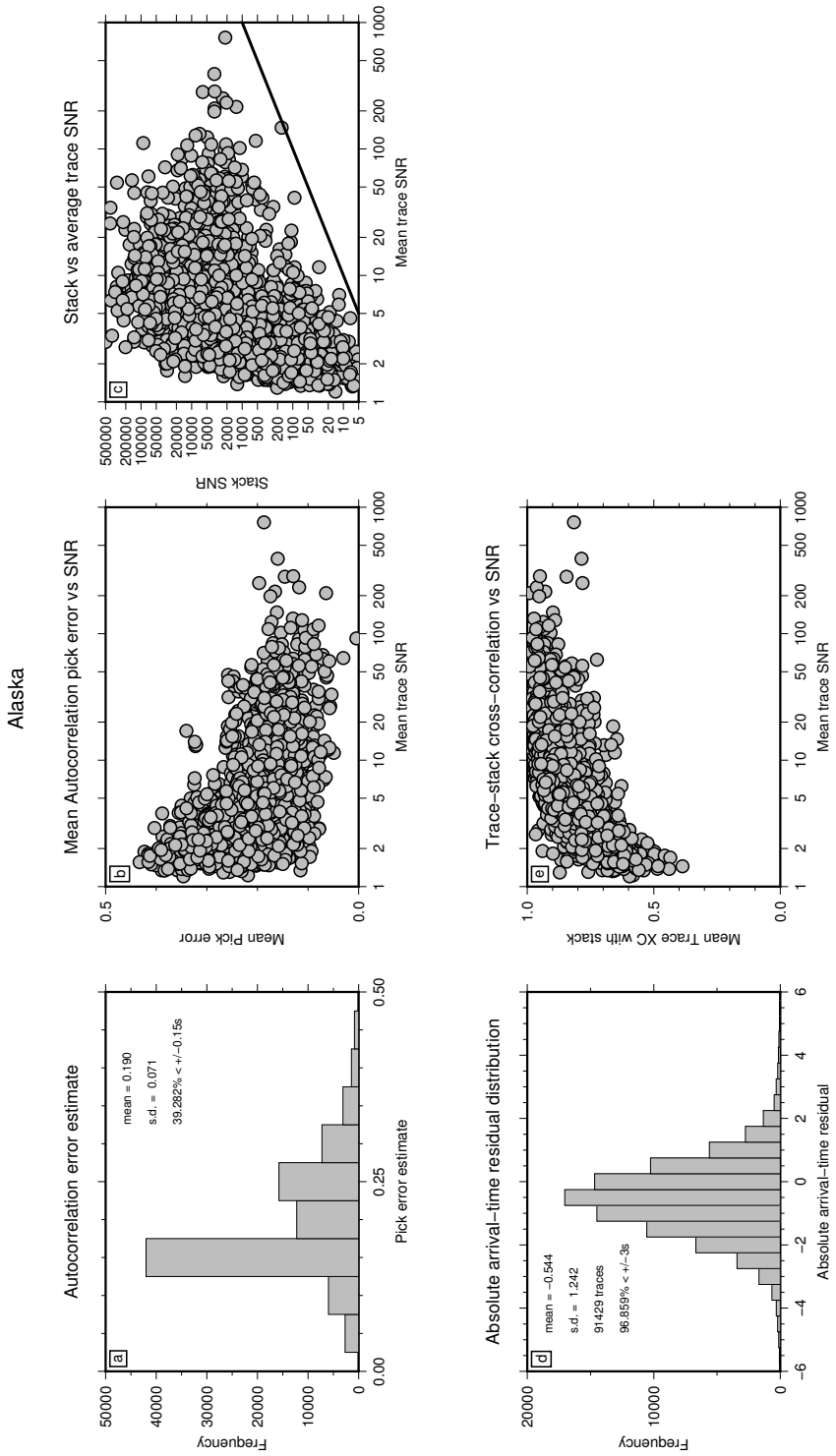

Figure S13. For the Alaskan land-station data set: (*a*) Distribution of autocorrelation pick error estimates for each arrival-time. (*b*) Mean autocorrelation pick error against mean trace SNR for each earthquake. (*c*) Stacked trace SNR against mean trace SNR for each earthquake. Line y=x (black line). (*d*) Distribution of absolute arrival-time residuals. (*e*) Mean cross-correlation coefficient of each trace with the stack against mean trace SNR for each earthquake.

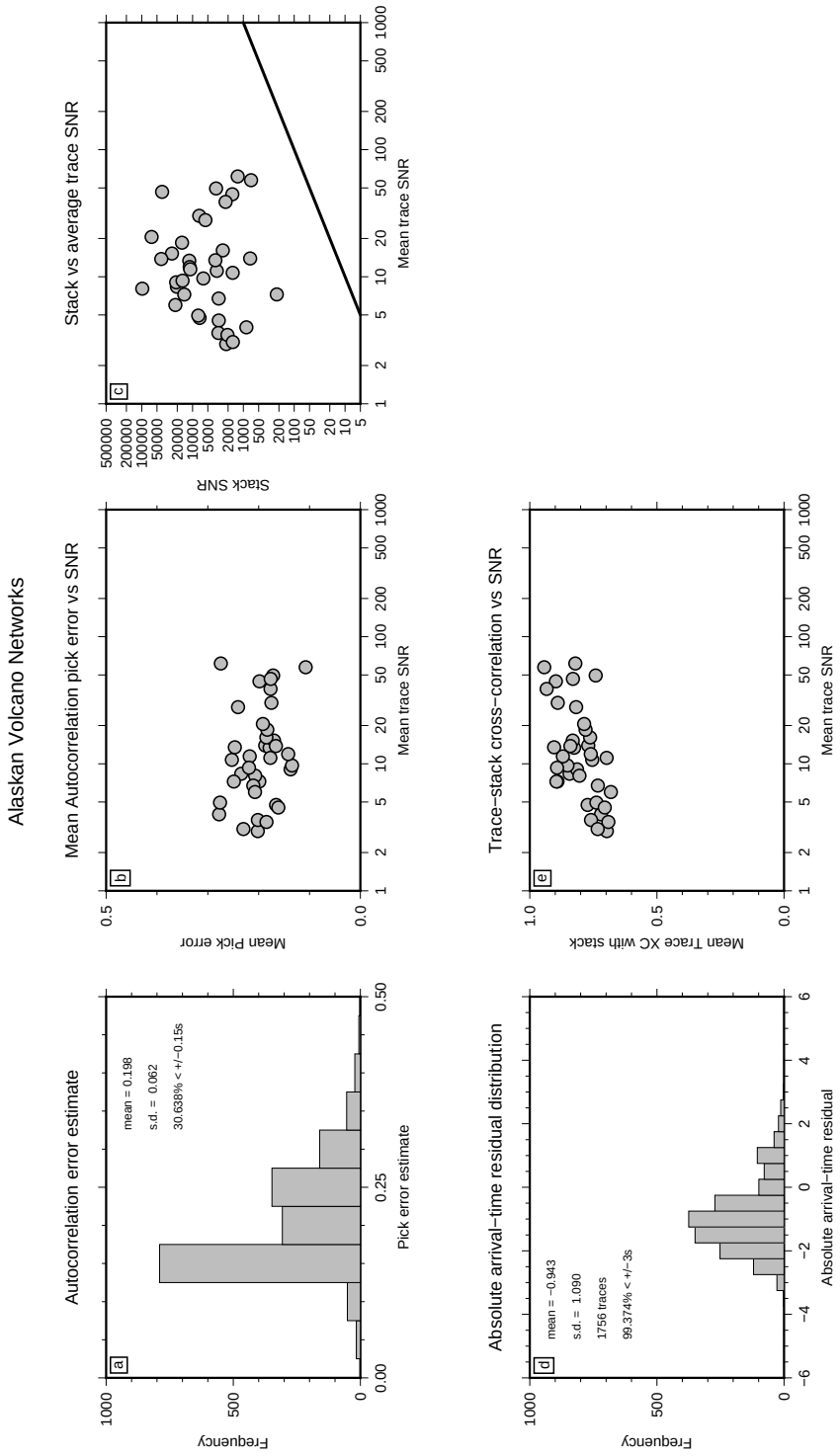

Figure S14. For the Alaskan volcano network (ALV) data set: (*a*) Distribution of autocorrelation pick error estimates for each arrival-time. (*b*) Mean autocorrelation pick error against mean trace SNR for each earthquake. (*c*) Stacked trace SNR against mean trace SNR for each earthquake. Line y=x (black line). (*d*) Distribution of absolute arrival-time residuals. (*e*) Mean cross-correlation coefficient of each trace with the stack against mean trace SNR for each earthquake.

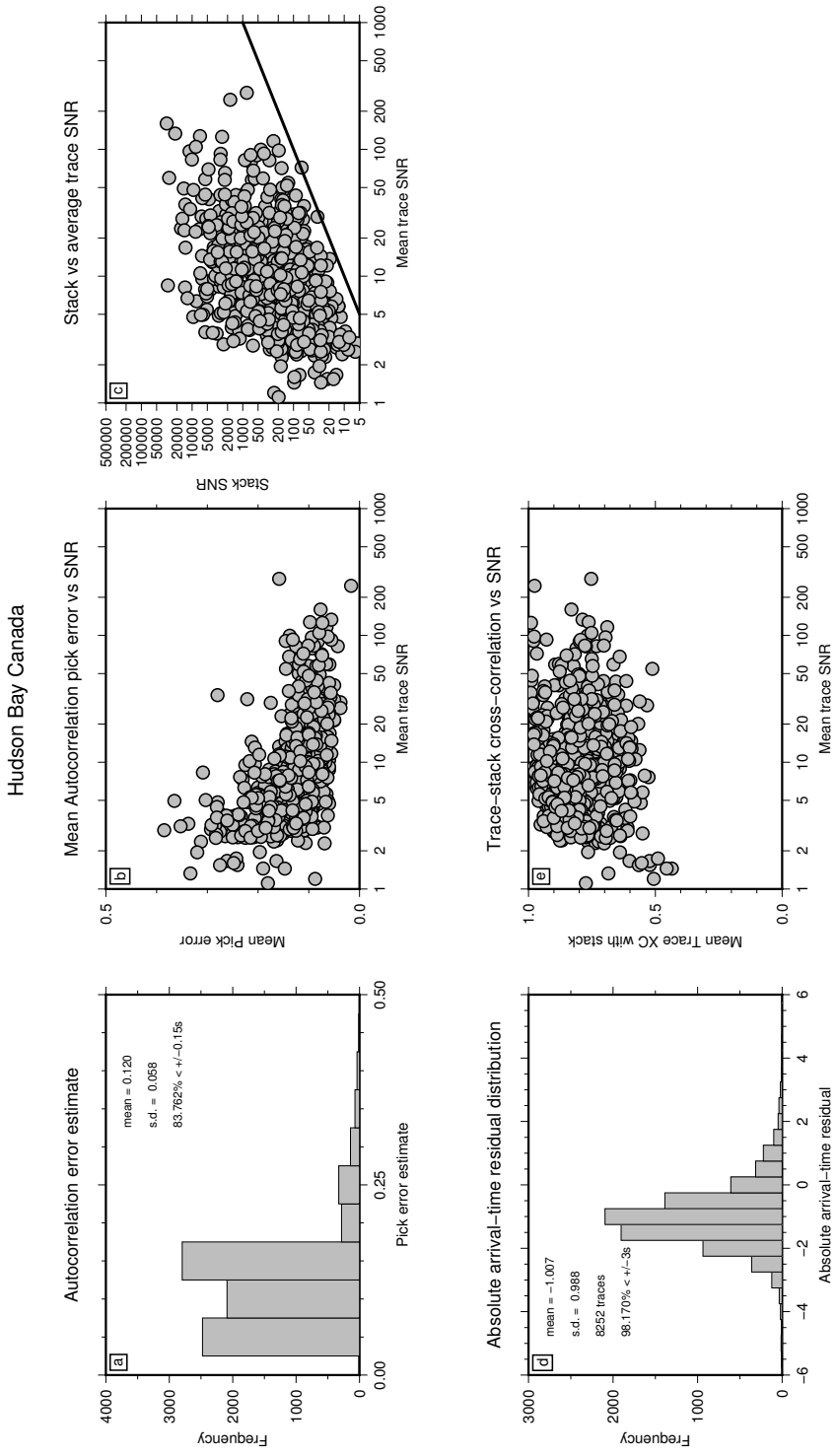

Figure S15. For the Hudson Bay data set: (*a*) Distribution of autocorrelation pick error estimates for each arrival-time. (*b*) Mean autocorrelation pick error against mean trace SNR for each earthquake. (*c*) Stacked trace SNR against mean trace SNR for each earthquake. Line y=x (black line). (*d*) Distribution of absolute arrival-time residuals. (*e*) Mean cross-correlation coefficient of each trace with the stack against mean trace SNR for each earthquake.

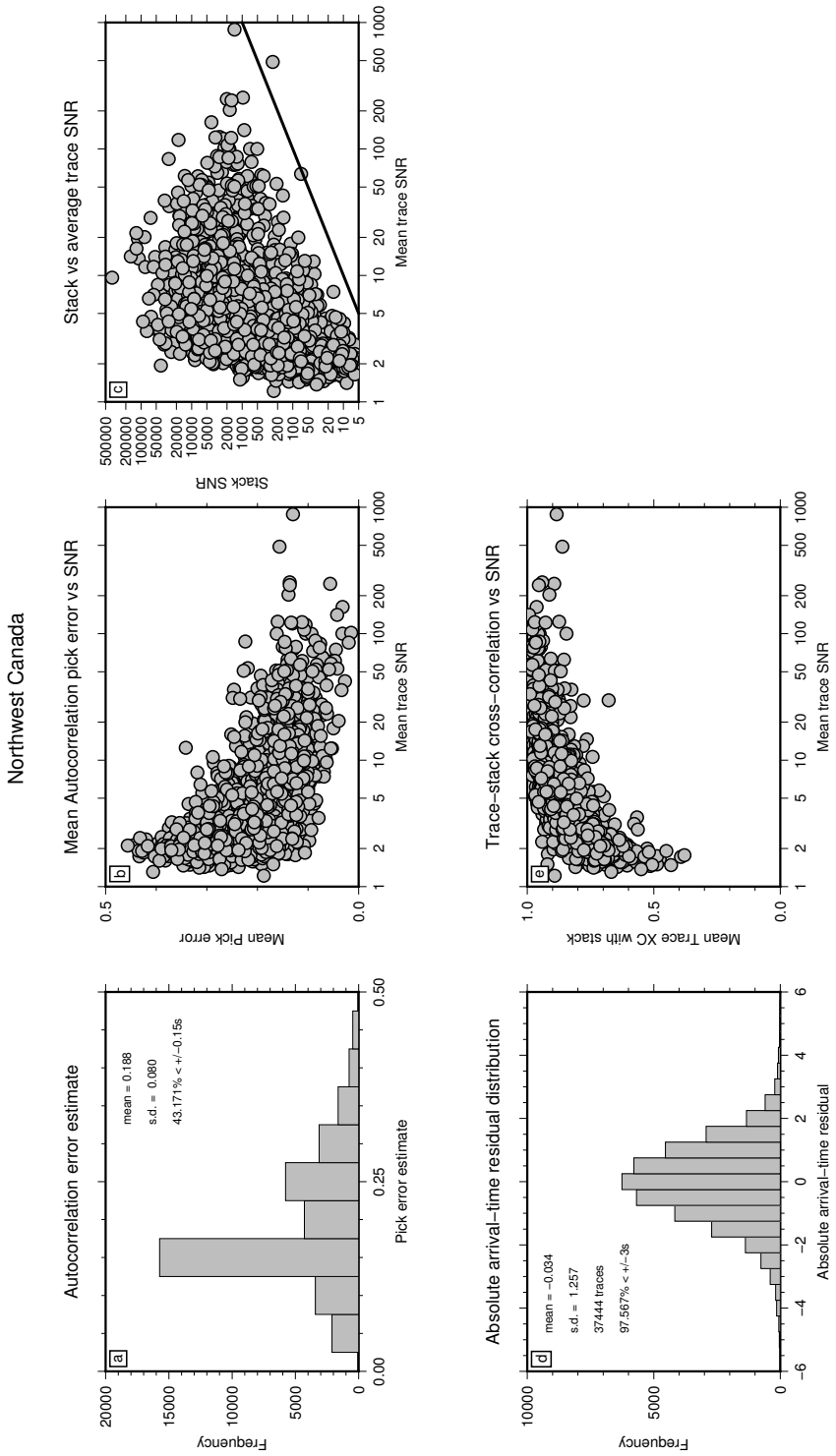

Figure S16. For the Northwest Canadian data set: (*a*) Distribution of autocorrelation pick error estimates for each arrival-time. (*b*) Mean autocorrelation pick error against mean trace SNR for each earthquake. (*c*) Stacked trace SNR against mean trace SNR for each earthquake. Line y=x (black line). (*d*) Distribution of absolute arrival-time residuals. (*e*) Mean cross-correlation coefficient of each trace with the stack against mean trace SNR for each earthquake.

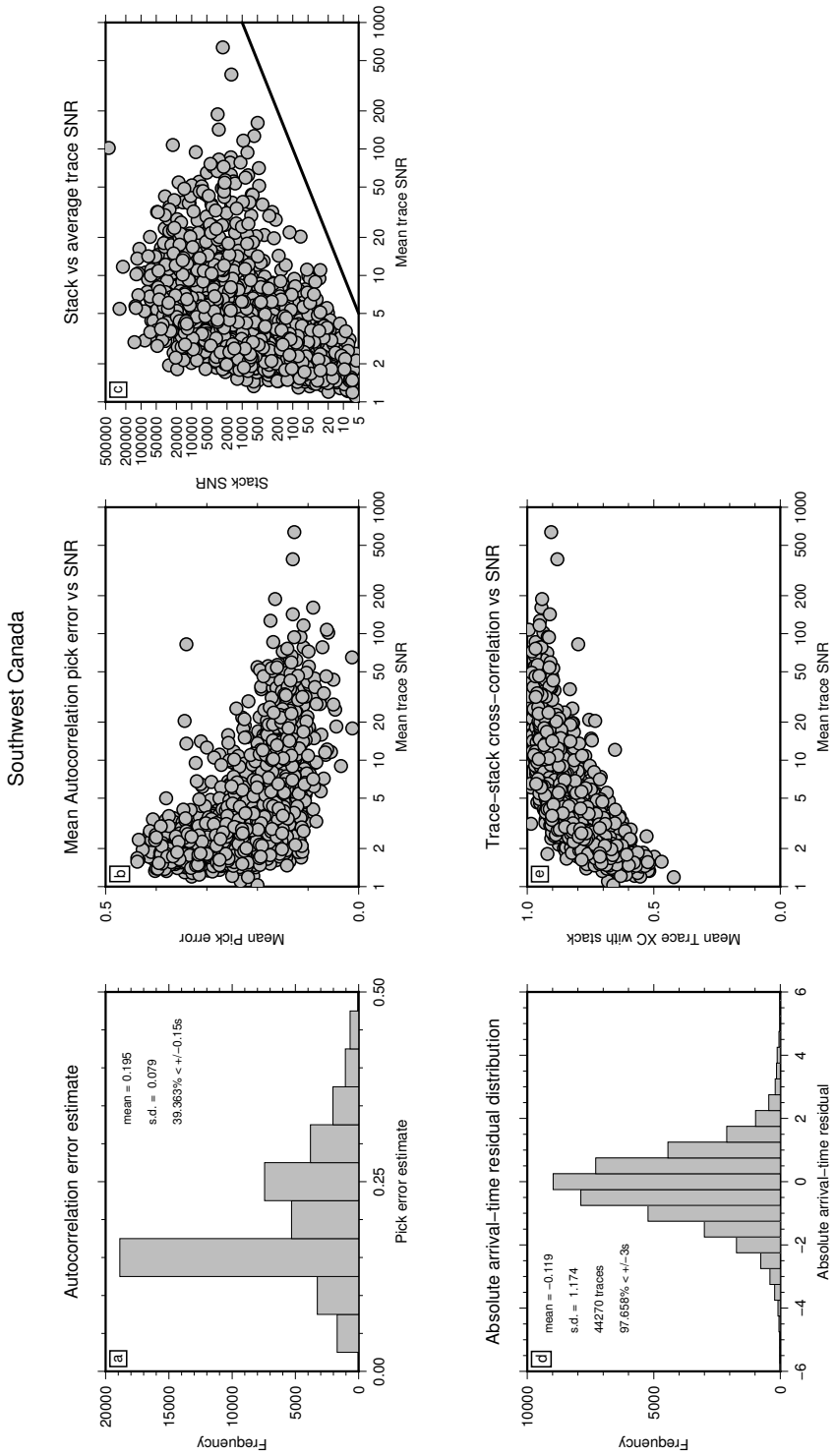

Figure S17. For the Southwest Canadian data set: (*a*) Distribution of autocorrelation pick error estimates for each arrival-time. (*b*) Mean autocorrelation pick error against mean trace SNR for each earthquake. (*c*) Stacked trace SNR against mean trace SNR for each earthquake. Line y=x (black line). (*d*) Distribution of absolute arrival-time residuals. (*e*) Mean cross-correlation coefficient of each trace with the stack against mean trace SNR for each earthquake.

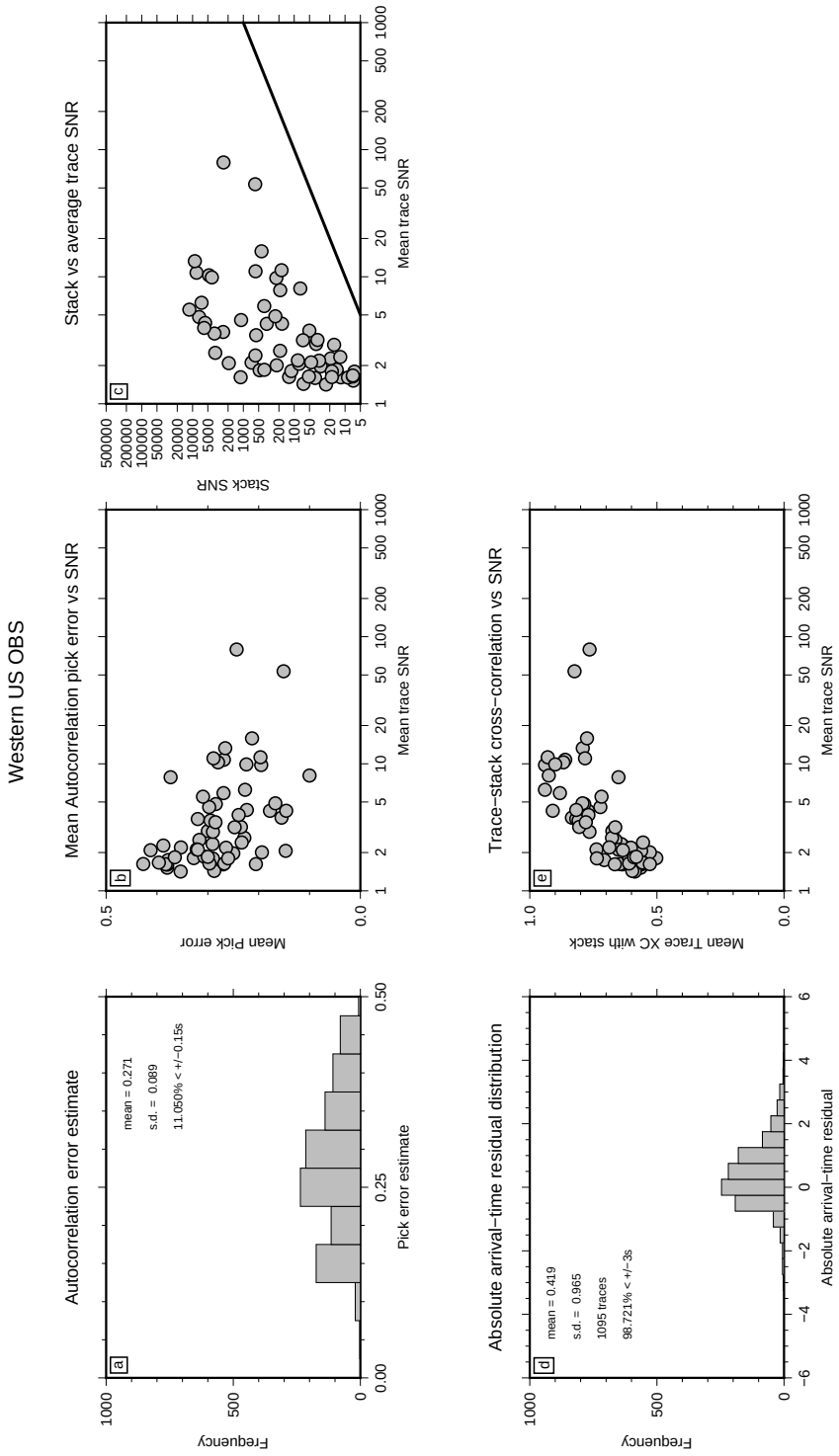

Figure S18. For the Western US (Cascadia) OBS set: (*a*) Distribution of autocorrelation pick error estimates for each arrival-time. (*b*) Mean autocorrelation pick error against mean trace SNR for each earthquake. (*c*) Stacked trace SNR against mean trace SNR for each earthquake. Line y=x (black line). (*d*) Distribution of absolute arrival-time residuals. (*e*) Mean cross-correlation coefficient of each trace with the stack against mean trace SNR for each earthquake.

Coordinate Transformation and Adaptive Parameterization

To limit the impact of converging lines of longitude at high latitudes within Alaska and northern Canada, immediately prior to tomographic inversion we employ a coordinate transformation to move North America to equatorial latitudes (Figure S19). The resulting adaptively parameterized grid of cells within the inversion is displayed at four depths (*a*–*d*: 100–600 km) in Figure S20. Cells are plotted as fine black lines over the CAP22 tomographic model.

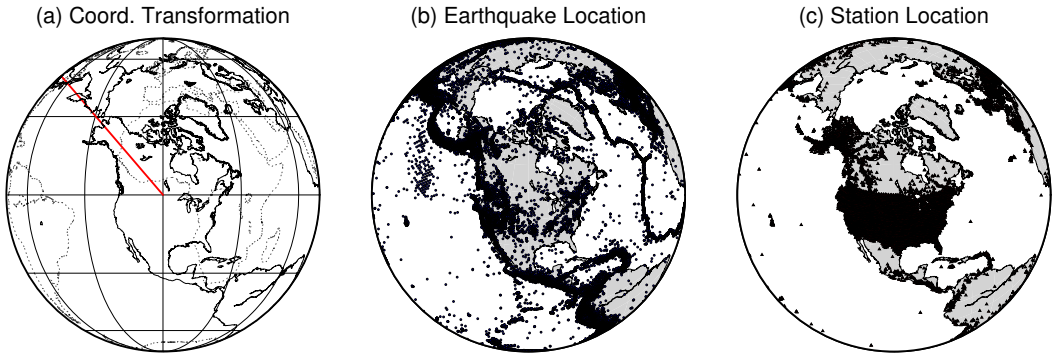

Figure S19. Through the applied data coordinate transformation (a) a point in central North America (100°W, 49°N) is moved to (0°E,0°N) following the red line. Coastlines pre- (dashed) and post-transformation (solid) are shown. Global distribution of earthquakes (b) and stations (c) after coordinate transformation.

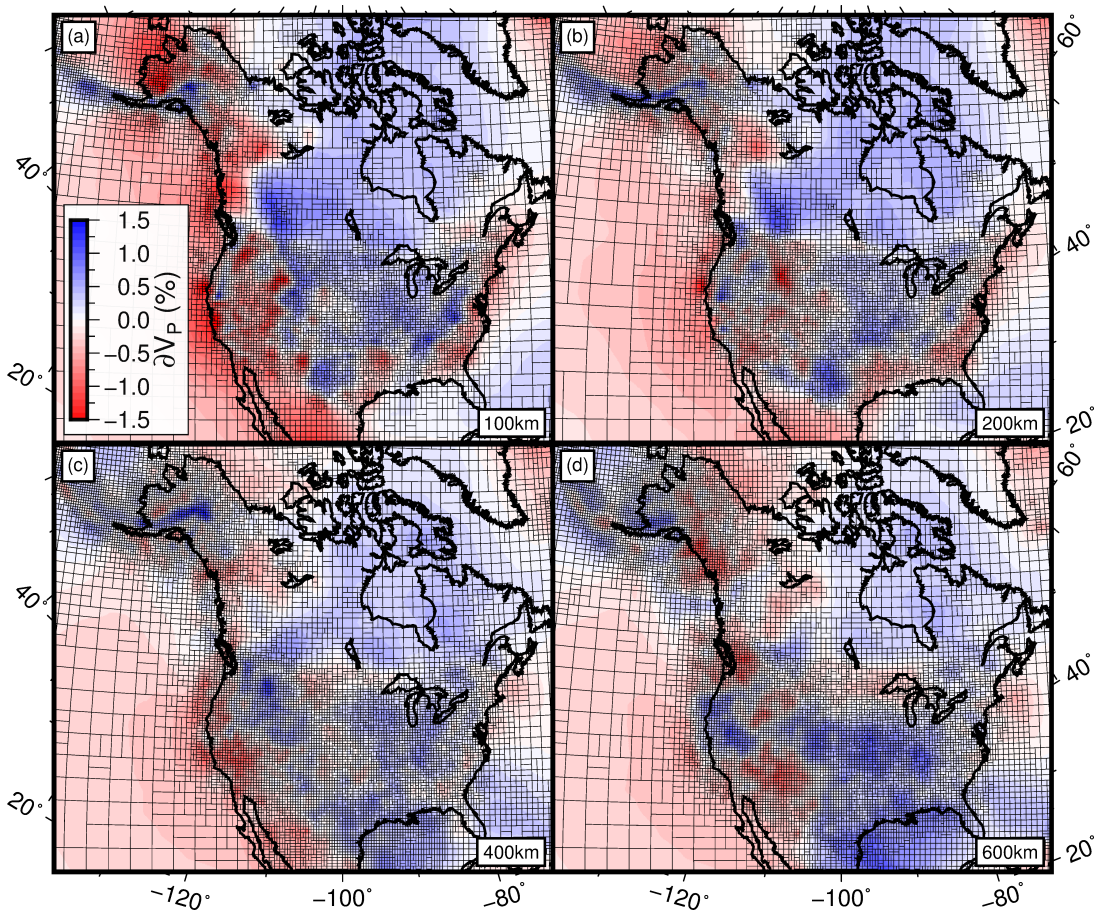

Figure S20. The adaptively parameterized grid used in the inversion for CAP22 tomographic model is indicated by fine black cells at four depths (*a*–*d*: 100–600 km) after coordinate transformation (Figure S19). Wavespeed anomalies are plotted as percentage deviation from ak135 (δV_P=±1.5%).

Trade-off Curve Approach

We use a trade-off curve determine the horizontal- and vertical-gradient smoothing parameters in CAP22 (Figure S21). The model damping parameter (N) has very limited impact on the resulting model around the knee of the trade-off curve. The preferred model "E" lies near the knee of both curves in the global parameterization and has regularization values of $H = 4000$, $R = 1000$ and $N = 50$. Trade-off parameters are shown in Tables S1–S3.

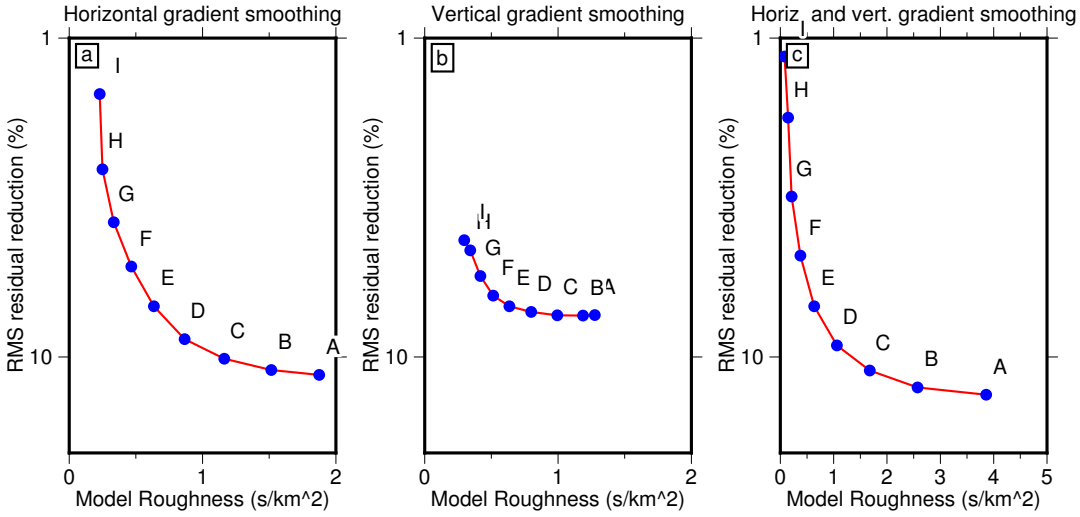

Figure S21. Horizontal (a), vertical (b), combined horizontal and vertical (c), gradient smoothing parameters used in the inversion for CAP22 are determined through a trade-off curve approach. Root-mean-squared residual reduction (%) is plotted against model roughness (s/km^2). We choose model "E". Absolute values can be found in Tables S1–S3.

Horizontal Gradient Smoothing				
Label	H	R	Roughness	RMS res. Red.
A	250	1000	1.87513	11.3873
B	500	1000	1.51540	10.9917
C	1000	1000	1.16309	10.1283
D	2000	1000	0.86519	8.79167
E	4000	1000	0.63525	6.9355
F	8000	1000	0.46610	5.20324
G	16000	1000	0.33421	3.77984
H	32000	1000	0.24970	2.58008
I	64000	1000	0.22863	1.49778

Table S1. Parameters from horizontal gradient smoothing (H) trade-off analysis corresponding to Figure S21a.

Vertical Gradient Smoothing				
Label	H	R	Roughness	RMS res. Red.
A	4000	62	1.27531	7.3903
B	4000	125	1.18764	7.42002
C	4000	250	0.99440	7.40066
D	4000	500	0.79882	7.22816
E	4000	1000	0.63525	6.9355
F	4000	2000	0.51334	6.42004
G	4000	4000	0.41755	5.57791
H	4000	8000	0.34138	4.63276
I	4000	16000	0.29671	4.30321

Table S2. Parameters from vertical gradient smoothing (R) trade-off analysis corresponding to Figure S21b.

Horizontal and Vertical Gradient Smoothing				
Label	H	R	Roughness	RMS res. Red.
A	4000	62	1.27531	7.3903
B	4000	125	1.18764	7.42002
C	4000	250	0.99440	7.40066
D	4000	500	0.79882	7.22816
E	4000	1000	0.63525	6.9355
F	4000	2000	0.51334	6.42004
G	4000	4000	0.41755	5.57791
H	4000	8000	0.34138	4.63276
I	4000	16000	0.29671	4.30321

Table S3. Parameters from combined horizontal (H) and vertical (R) gradient smoothing trade-off analysis corresponding to Figure S21c.

Additional Checkerboard Resolution Tests

We distribute alternating $\delta V_P = \pm 2\%$ wavespeed anomalies of 300 km thickness throughout the model space at 200 km, 500 km and 800 km depth to form the input to additional checkerboard resolution tests. We test lateral anomaly length scales of 10° below the entirety of North America and additionally length scales of 1–2° below Alaska (Figures S22–S24). Discussion of these tests is found in Section 2.3 of the main manuscript. We calculate arrival-time residuals through synthetic wavespeed models using identical ray paths to the observed data and add 0.2 s standard deviation Gaussian noise before inversion.

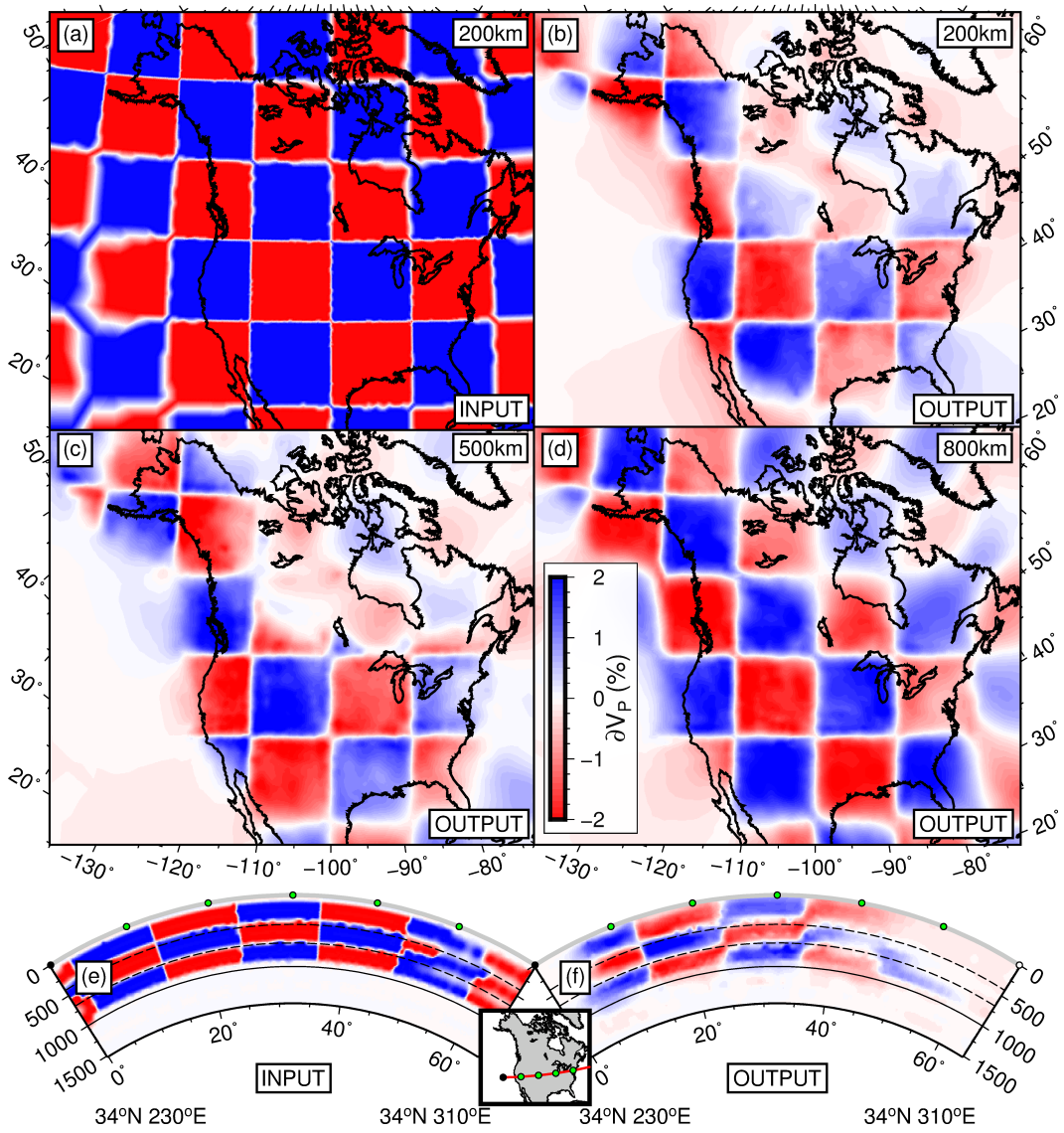

Figure S22. Checkerboard resolution tests using $\delta V_P = \pm 2.0\%$ input wavespeed anomalies of 10° width. Positive and negative input anomalies arranged in an alternating grid centered at 200 km, 500 km and 800 km depth are displayed in map (*a*) and cross section along the W-E profile (*e*). Visual defects within the input anomaly model result from a coarse adaptive grid in poorly sampled regions (Figure S20). Recovered anomalies (*b–d,f*) are displayed on the same color scale as the input.

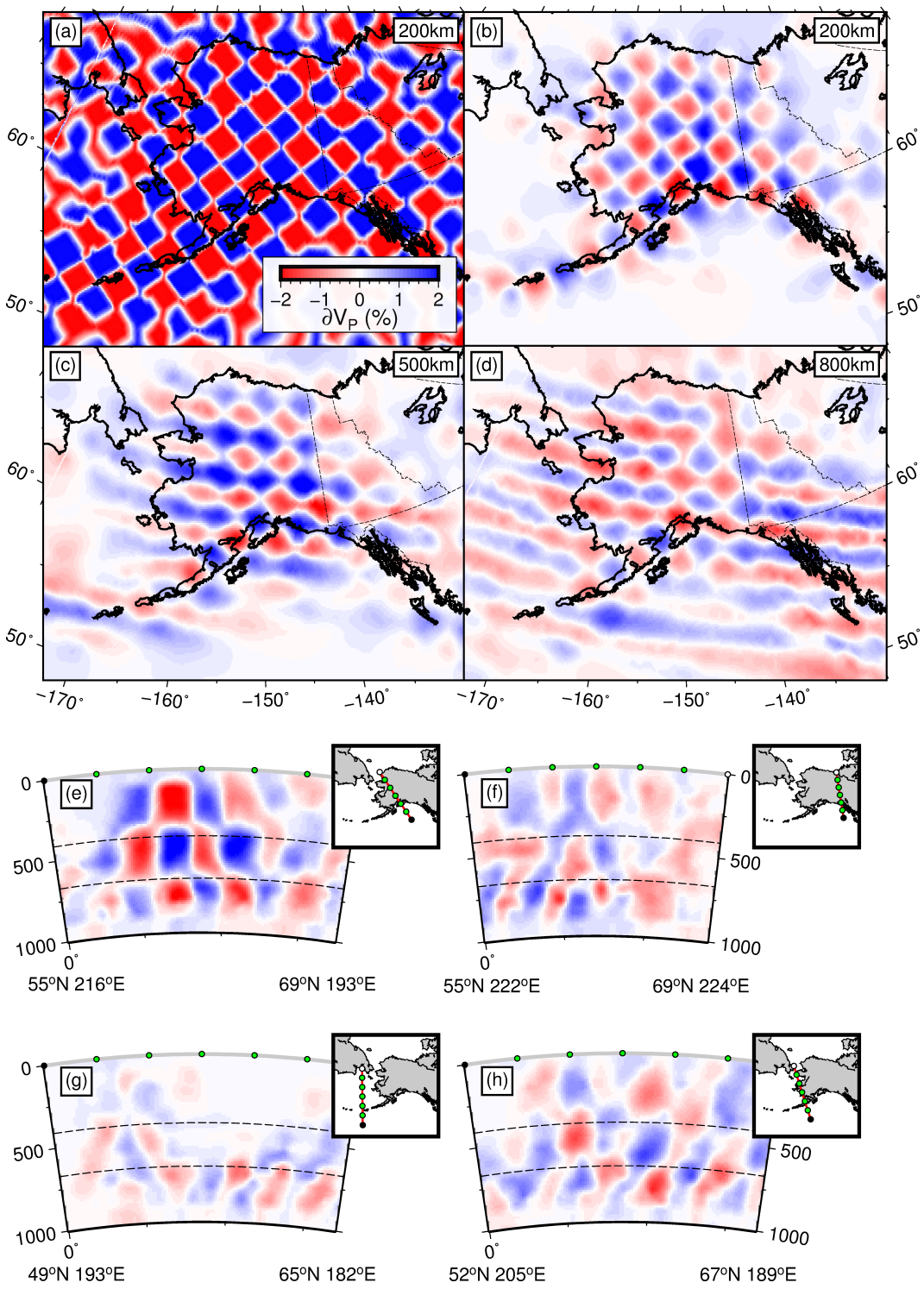

Figure S23. Checkerboard resolution tests shown for Alaska using $\delta V_P = \pm 2.0\%$ input wavespeed anomalies of 2° width. Positive and negative input anomalies arranged in an alternating grid centered at 200 km, 500 km and 800 km depth are displayed in map view (a). Visual defects within the input anomaly model result from a coarse adaptive grid in poorly sampled regions (Figure S20). Recovered anomalies (b–h) are displayed on the same color scale as the input. We use the same cross-sections as Figure 11 in the main manuscript to assist comparison.

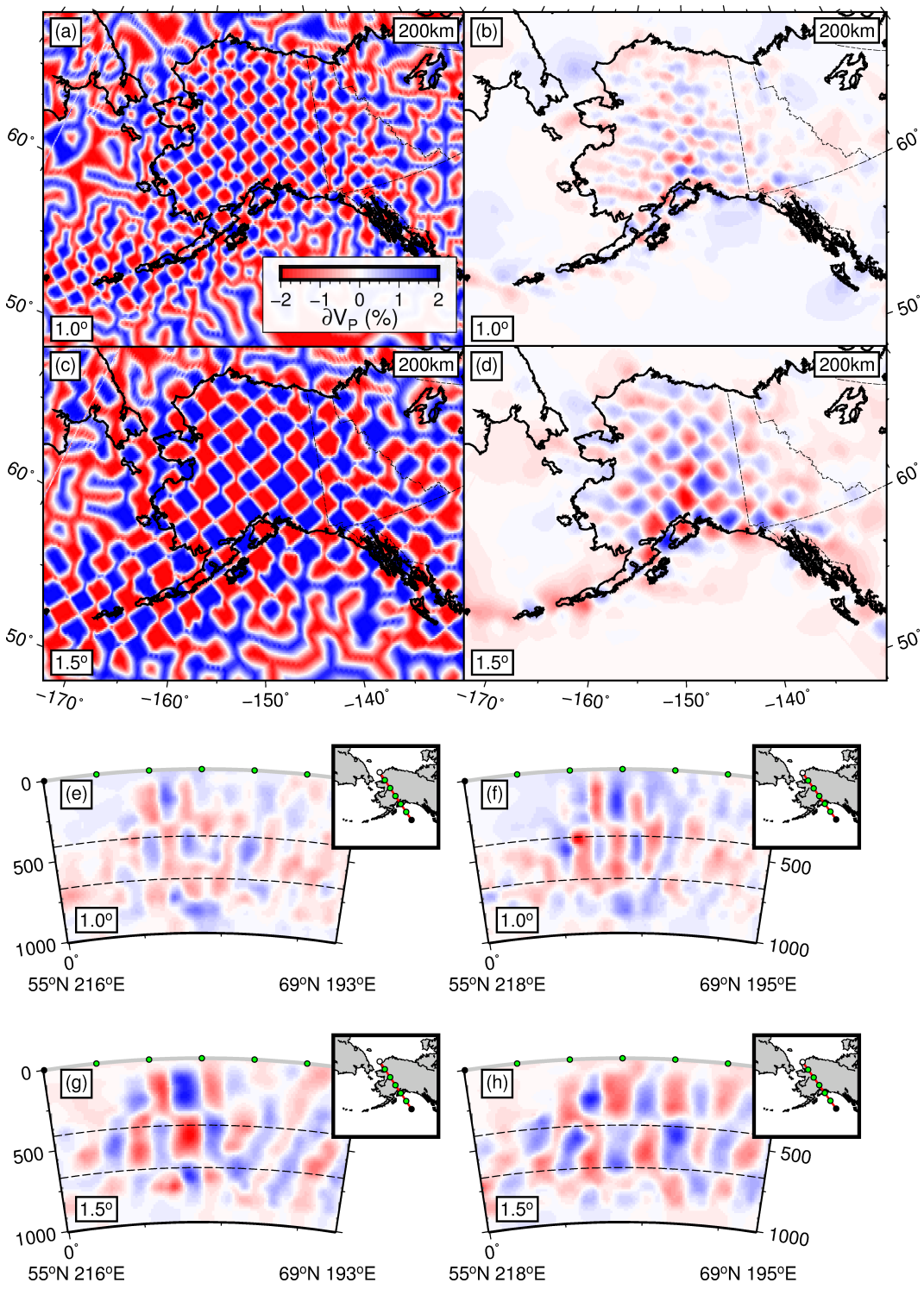

Figure S24. Fine-scale checkerboard resolution tests shown for Alaska using $\delta V_P = \pm 2.0\%$ input wavespeed anomalies of 1.0° and 1.5° width (size shown in lower left of each sub figure). Positive and negative input anomalies arranged in an alternating grid centered at 200 km, 500 km and 800 km depth are displayed in map view (a,c). Visual defects within the input anomaly model result from a coarse adaptive grid in poorly sampled regions (Figure S20). Recovered anomalies (b,d–h) are displayed on the same color scale as the input. Cross sections intersect Denali Volcanic Gap (DVG: see main manuscript).

References

Abers, G., Wiens, D., Schwartz, S., Sheehan, A., Shillington, D., Worthington, L., ... Adams, A. (2018). *AACSE: Alaska Amphibious Community seismic Experiment* [data set]. International Federation of Digital Seismograph Networks. (Seismic Network) doi: 10.7914/SN/XO_2018

Alaska Earthquake Center, Univ. of Alaska Fairbanks. (1987). *Alaska Regional Network* [data set]. International Federation of Digital Seismograph Networks. Retrieved from `https://www.fdsn.org/networks/detail/AK/` (Seismic Network) doi: 10.7914/SN/AK

Alaska Volcano Observatory/USGS. (1988). *Alaska Volcano Observatory* [data set]. International Federation of Digital Seismograph Networks. Retrieved from `https://www.fdsn.org/networks/detail/AV/` (Seismic Network) doi: 10.7914/SN/AV

Alberta Geological Survey / Alberta Energy Regulator. (2013). *Regional Alberta Observatory for Earthquake Studies Network* [data set]. International Federation of Digital Seismograph Networks. Retrieved from `https://www.fdsn.org/networks/detail/RV/` (Seismic Network) doi: 10.7914/SN/RV

Albuquerque Seismological Laboratory (ASL)/USGS. (1990). *United States National Seismic Network* [data set]. International Federation of Digital Seismograph Networks. Retrieved from `https://www.fdsn.org/networks/detail/US/` (Seismic Network) doi: 10.7914/SN/US

Albuquerque Seismological Laboratory/USGS. (2014). *Global Seismograph Network (GSN - IRIS/USGS)* [data set]. International Federation of Digital Seismograph Networks. Retrieved from `https://www.fdsn.org/networks/detail/IU/` (Seismic Network) doi: 10.7914/SN/IU

Babaie Mahani, A., Esfahani, F., Kao, H., Gaucher, M., Hayes, M., Visser, R., & Venables, S. (2019). A Systematic Study of Earthquake Source Mechanism and Regional Stress Field in the Southern Montney Unconventional Play of Northeast British Columbia, Canada. *Seis. Res. Lett.*, *91*(1), 195-206. doi: 10.1785/0220190230

Baker, M. G., Heath, D. C., Schutt, D. L., Aster, R. C., Cubley, J. F., & Freymueller, J. T. (2020). The Mackenzie Mountains EarthScope Project: Studying

Active Deformation in the Northern North American Cordillera from Margin to Craton. *Seism. Res. Lett.*, *91*, 521–532. doi: 10.1785/0220190139

Barcheck, G., Abers, G. A., Adams, A. N., Bécel, A., Collins, J., Gaherty, J. B., ... Worthington, L. L. (2020). The Alaska Amphibious Community Seismic Experiment. *Seis. Res. Lett.*, *91*(6), 3054-3063. doi: 10.1785/0220200189

Bastow, I. D., Eaton, D. W., Kendall, J., Helffrich, G., Snyder, D. B., Thompson, D. A., ... Pawlak, A. E. (2015). The Hudson Bay Lithospheric Experiment (HuBLE): insights into Precambrian plate tectonics and the development of mantle keels. *Geol. Soc. Lond. Spec. Pub.*, *389*(1), 41–67. doi: 10.1144/SP389.7

Bent, A. L., Côté, T. J., Seywerd, H. C. J., McCormack, D. A., & Coyle, K. A. (2019). The Canadian National Seismograph Network: Upgrade and Status. *Seis. Res. Lett.*, *91*(2A), 585-592. doi: 10.1785/0220190202

Berger, A. L., Gulick, S. P. S., Spotila, J. A., Upton, P., Jaeger, J. M., Chapman, J. B., ... others (2008). Quaternary tectonic response to intensified glacial erosion in an orogenic wedge. *Nature Geoscience*, *1*(11), 793–799. doi: 10.1038/ngeo334

Boggs, K. J. E., Aster, R. C., Audet, P., Brunet, G., Clowes, R. M., de Groot-Hedlin, C. D., ... West, N. (2018, Jul.). EON-ROSE and the Canadian Cordillera Array – Building Bridges to Span Earth System Science in Canada. *Geoscience Canada*, *45*(2), 97–109. doi: 10.12789/geocanj.2018.45.136

Boyce, A., Bastow, I. D., Cottaar, S., Kounoudis, R., Guilloud De Courbeville, J., Caunt, E., & Desai, S. (2021). AFRP20: New P-wavespeed Model for the African Mantle Reveals Two Whole-Mantle Plumes Below East Africa and Neoproterozoic Modification of the Tanzania Craton. *Geochem. Geophys. Geosyst.*, *22*(3). doi: 10.1029/2020GC009302

Boyce, A., Bastow, I. D., Darbyshire, F. A., Ellwood, A. G., Gilligan, A., Levin, V., & Menke, W. (2016). Subduction beneath Laurentia modified the eastern North American cratonic edge: Evidence from P wave and S wave tomography. *J. Geophys. Res.*, *121*(7), 5013–5030. doi: 10.1002/2016JB012838

Boyce, A., Bastow, I. D., Golos, E. M., Rondenay, S., Burdick, S., & Van der Hilst, R. D. (2019). Variable modification of continental lithosphere during the Proterozoic Grenville orogeny: Evidence from teleseismic P-wave tomography.

Earth Planet. Sci. Lett., *525*, 115763. doi: 10.1016/j.epsl.2019.115763

Boyce, A., Bastow, I. D., Rondenay, S., & Van der Hilst, R. D. (2017). From relative to absolute teleseismic travel-times: the Absolute Arrival-time Recovery Method (AARM). *Bull. Seis. Soc. Am.*, *107*(5), 2511—2520. doi: 10.1785/0120170021

Burdick, S., Vernon, F. L., Martynov, V., Eakins, J., Cox, T., Tytell, J., ... Van der Hilst, R. D. (2017). Model Update May 2016: Upper-Mantle Heterogeneity beneath North America from Travel-Time Tomography with Global and USArray Data. *Seis. Res. Lett.*, *88*(2A), 319–325. doi: 10.1785/0220160186

Calkins, J. A., Zandt, G., Girardi, J., Dueker, K., Gehrels, G. E., & Ducea, M. N. (2010). Characterization of the crust of the Coast Mountains Batholith, British Columbia, from P to S converted seismic waves and petrologic modeling. *Earth Planet. Sci. Lett.*, *289*(1), 145-155. doi: https://doi.org/10.1016/j.epsl.2009.10.037

Cui, L., & Atkinson, G. M. (2016). Spatiotemporal Variations in the Completeness Magnitude of the Composite Alberta Seismicity Catalog (CASC). *Seis. Res. Lett.*, *87*(4), 853-863. doi: 10.1785/0220150268

Dixon, J., Stihler, S., Power, J., Haney, M., Parker, T., Searcy, C., & Prejean, S. (2013). *Catalog of earthquake hypocenters at Alaskan volcanoes: January 1 through December 31, 2012* [data set]. U.S. Geological Survey Data Series 789, 84 p. Retrieved from `https://pubs.usgs.gov/ds/789/`

Dueker, K., & Zandt, G. (2005). *Magma Accretion and the Formation of Batholiths* [data set]. International Federation of Digital Seismograph Networks. Retrieved from `https://www.fdsn.org/networks/detail/XY_2005/` (Seismic Network) doi: 10.7914/SN/XY_2005

D'Alessandro, A., & Ruppert, N. A. (2012). Evaluation of Location Performance and Magnitude of Completeness of the Alaska Regional Seismic Network by the SNES Method. *Bull. Seis. Soc. Am.*, *102*(5), 2098-2115. doi: 10.1785/0120110199

Eaton, D., Frederiksen, A., & Miong, S. (2004). Shear-wave splitting observations in the lower Great Lakes region: Evidence for regional anisotropic domains and keel-modified asthenospheric flow. *Geophys. Res. Lett.*, *31*(7), 4. doi: 10.1029/2004GL019438

Engdahl, E. R., Van der Hilst, R. D., & Buland, R. (1998). Global teleseismic earthquake relocation with improved travel times and procedures for depth determination. *Bull. Seis. Soc. Am.*, *88*(3), 722–743.

Estève, C., Audet, P., Schaeffer, A. J., Schutt, D. L., Aster, R. C., & Cubley, J. (2020). The Upper Mantle Structure of Northwestern Canada From Teleseismic Body Wave Tomography. *J. Geophys. Res.*, *125*(2). doi: 10.1029/2019jb018837

Estève, C., Schaeffer, A. J., & Audet, P. (2019). Upper mantle structure underlying the diamondiferous Slave craton from teleseismic body-wave tomography. *Tectonophysics*, *757*, 187–202. doi: 10.1016/j.tecto.2019.01.012

Gaherty, J., & Revenaugh, J. (2003). *Collaborative Research: Canadian Northwest Seismic Experiment* [data set]. International Federation of Digital Seismograph Networks. Retrieved from `https://www.fdsn.org/networks/detail/XN_2003/` (Seismic Network) doi: 10.7914/SN/XN_2003

Geological Survey of Canada. (2000). *Portable Observatories for Lithospheric Analysis and Research Investigating Seismicity (POLARIS)* [data set]. International Federation of Digital Seismograph Networks. Retrieved from `http://www.polarisnet.ca/network/polaris-network-locations.html` (Seismic Network)

Gu, Y. J., Okeler, A., Shen, L., & Contenti, S. (2011). The Canadian Rockies and Alberta Network (CRANE): New constraints on the Rockies and western Canada sedimentary basin. *Seis. Res. Lett.*, *82*(4), 575–588. doi: 10.1785/gssrl.82.4.575

Hansen, R., & Pavlis, G. (2005). *Collaborative Research: St. Elias Erosion/Tectonics Project* [data set]. International Federation of Digital Seismograph Networks. Retrieved from `https://www.fdsn.org/networks/detail/XZ_2005/` (Seismic Network) doi: 10.7914/SN/XZ_2005

Indiana University Bloomington (IU Bloomington). (1998). *PEPP-Indiana* [data set]. International Federation of Digital Seismograph Networks. Retrieved from `https://www.fdsn.org/networks/detail/PN/` (Seismic Network)

IRIS OBSIP. (2011). *Cascadia Initiative Community Experiment - OBS Component* [data set]. International Federation of Digital Seismograph Networks. (Seismic Network) doi: 10.7914/SN/7D_2011

Keranen, K. (2011). *Broadband recording at the site of great earthquake rupture in the Alaska Megathrust* [data set]. International Federation of Digital Seismograph Networks. Retrieved from `https://www.fdsn.org/networks/detail/XM_2011/` (Seismic Network) doi: 10.7914/SN/XM_2011

Larsen, C., & Truffer, M. (2007). *Glacier Seismicity and High Resolution Motion Records: Relation to Glacier Erosion* [data set]. International Federation of Digital Seismograph Networks. Retrieved from `https://www.fdsn.org/networks/detail/XV_2007/` (Seismic Network) doi: 10.7914/SN/XV_2007

Li, C., Van der Hilst, R. D., Engdahl, R., & Burdick, S. (2008). A new global model for P wave speed variations in Earth's mantle. *Geochem. Geophys. Geosyst.*, *9*(5). doi: 10.1029/2007GC001806

Liddell, M. V., Bastow, I. D., Rawlinson, N., Darbyshire, F. A., Gilligan, A., & Watson, E. (2018). Precambrian Plate Tectonics in Northern Hudson Bay: Evidence from P and S-wave Seismic Tomography and Analysis of Source Side Effects in Relative Arrival-Time Datasets. *J. Geophys. Res.*, *123*(7), 5690–5709. doi: 10.1029/2018jb015473

McGill University (Canada). (2017). *McGill Dawson-Septimus Induced Seismicity Study* [data set]. International Federation of Digital Seismograph Networks. Retrieved from `https://www.fdsn.org/networks/detail/XL_2017/` (Seismic Network)

Mercier, J.-P., Bostock, M. G., Cassidy, J. F., Dueker, K., Gaherty, J. B., Garnero, E. J., ... Zandt, G. (2009). Body-wave tomography of western Canada. *Tectonophysics*, *475*(3-4), 480–492. doi: 10.1016/j.tecto.2009.05.030

Nabelek, J., & Braunmiller, J. (2012). *Plate Boundary Evolution and Physics at an Oceanic Transform Fault System* [data set]. International Federation of Digital Seismograph Networks. (Seismic Network) doi: 10.7914/SN/X9_2012

Nabelek, J., & Braunmiller, J. (2013). *Seismicity, Structure and Dynamics of the Gorda Deformation Zone* [data set]. International Federation of Digital Seismograph Networks. (Seismic Network) doi: 10.7914/SN/Z5_2013

Natural Resources Canada (NRCAN Canada). (1975). *Canadian National Seismograph Network* [data set]. International Federation of Digital Seismograph Networks. Retrieved from `https://www.fdsn.org/networks/detail/CN/` (Seismic Network) doi: 10.7914/SN/CN

Natural Resources Canada (NRCAN Canada). (2002). *Canadian Seismic Research Network* [data set]. International Federation of Digital Seismograph Networks. Retrieved from `http://www.earthquakescanada.nrcan.gc.ca/stndon/` (Seismic Network)

Natural Resources Canada (NRCAN Canada). (2018). *GSC-BCOGC Induced Seismicity Study* [data set]. International Federation of Digital Seismograph Networks. Retrieved from `https://www.fdsn.org/networks/detail/1E_2018/` (Seismic Network)

NOAA National Oceanic and Atmospheric Administration (USA). (1967). *National Tsunami Warning Center Alaska Seismic Network* [data set]. International Federation of Digital Seismograph Networks. Retrieved from `https://www.fdsn.org/networks/detail/AT/` (Seismic Network) doi: 10.7914/SN/AT

North, R. G. (1994). The Canadian Nation Seismograph Network. *Annales de Geophys.*, *37*(5), 1045-1048.

Oppenheimer, D. H., Bittenbinder, A. N., Bogaert, B. M., Buland, R. P., Dietz, L. D., Hansen, R. A., ... Weaver, C. S. (2005). The Seismic Project of the National Tsunami Hazard Mitigation Program. *Natural Hazards*, *35*, 59–72. doi: 10.1007/s11069-004-2404-2

Ringler, A. T., Anthony, R. E., Wilson, D. C., Auerbach, D., Bargabus, S., Davis, P., ... Klimczak, E. (2021). A Review of Timing Accuracy across the Global Seismographic Network. *Seis. Res. Lett.*, *92*(4), 2270-2281. doi: 10.1785/0220200394

Roth, M. P., Verdecchia, A., Harrington, R. M., & Liu, Y. (2020). High-Resolution Imaging of Hydraulic-Fracturing-Induced Earthquake Clusters in the Dawson-Septimus Area, Northeast British Columbia, Canada. *Seis. Res. Lett.*, *91*(5), 2744-2756. doi: 10.1785/0220200086

Rutgers University. (2013). *Ocean Observatories Initiative* [data set]. International Federation of Digital Seismograph Networks. (Seismic Network) doi: 10.7914/SN/OO

Schultz, R., Stern, V., Gu, Y. J., & Eaton, D. (2015). Detection Threshold and Location Resolution of the Alberta Geological Survey Earthquake Catalogue. *Seis. Res. Lett.*, *86*(2A), 385-397. doi: 10.1785/0220140203

Schultz, R., Stern, V., & Yusifbayov, J. (2014). *Scientific Induced Seismicity Monitoring Network* [data set]. International Federation of Digital Seismograph Networks. Retrieved from `https://www.fdsn.org/networks/detail/2K_2014/` (Seismic Network) doi: 10.7914/SN/2K_2014

Schultz, R., Yusifbayov, J., & Shipman, T. (2020). *The Scientific Induced Seismicity Monitoring Network (SCISMN* [data set]. Alberta Energy Regulator / Alberta Geological Survey AER/AGS Open File Report 2019-09, 10 p. (Seismic Network)

Schutt, D. L., & Aster, R. C. (2015). *The Mackenzie Mountains Transect: Active Deformation from Margin to Craton* [data set]. International Federation of Digital Seismograph Networks. (Seismic Network) doi: 10.7914/SN/7C_2015

Scripps Institution of Oceanography. (1986). *Global Seismograph Network - IRIS/IDA* [data set]. International Federation of Digital Seismograph Networks. Retrieved from `https://www.fdsn.org/networks/detail/II/` (Seismic Network) doi: 10.7914/SN/II

Snyder, D. B., Bostock, M. G., & Lockhart, G. D. (2003). Two anisotropic layers in the Slave craton. *Lithos*, *71*(2), 529-539. doi: https://doi.org/10.1016/j.lithos.2003.09.001

Song, X., & Christensen, D. (2004). *CSEDI: Observational and Theoretical Constraints on the Structure and Rotation of the Inner Core* [data set]. International Federation of Digital Seismograph Networks. Retrieved from `https://www.fdsn.org/networks/detail/XR_2004/` (Seismic Network) doi: 10.7914/SN/XR_2004

Tape, C., Christensen, D., Moore-Driskell, M. M., Sweet, J., & Smith, K. (2017). Southern Alaska Lithosphere and Mantle Observation Network (SALMON): A Seismic Experiment Covering the Active Arc by Road, Boat, Plane, and Helicopter. *Seis. Res. Lett.*, *88*(4), 1185-1202. doi: 10.1785/0220160229

Tape, C., Christensen, D. H., & Moore-Driskell, M. M. (2015). *Southern Alaska Lithosphere and Mantle Observation Network* [data set]. International Federation of Digital Seismograph Networks. Retrieved from `https://www.fdsn.org/networks/detail/ZE_2015/` (Seismic Network) doi: 10.7914/SN/ZE_2015

Toomey, D. R., Allen, R. M., Barclay, A. H., Bell, S. W., Bromirski, P. D., Carlson,

R. L., ... others (2014). The Cascadia Initiative: A sea change in seismological studies of subduction zones. *Oceanography*, *27*(2), 138–150. doi: 10.5670/oceanog.2014.49

TransAlta Corporation. (2013). *TransAlta Monitoring Network* [data set]. International Federation of Digital Seismograph Networks. Retrieved from `http://www.transalta.com/` (Seismic Network)

University of Alberta (UAlberta Canada). (2006). *Canadian Rockies and Alberta Network (CRANE)* [data set]. International Federation of Digital Seismograph Networks. Retrieved from `https://www.fdsn.org/networks/detail/Y5_2006/` (Seismic Network)

University of Bristol (UK). (2007). *Hudson Bay Lithospheric Experiment (HUBLE)* [data set]. International Federation of Digital Seismograph Networks. Retrieved from `http://www.fdsn.org/networks/detail/X5_2007/` (Seismic Network)

University of Calgary (U of C Canada). (2018). *EON-ROSE* [data set]. International Federation of Digital Seismograph Networks. Retrieved from `https://www.fdsn.org/networks/detail/EO/` (Seismic Network) doi: 10.7914/SN/EO

University of Ottawa (uOttawa Canada). (2013). *Yukon-Northwest Seismic Network* [data set]. International Federation of Digital Seismograph Networks. Retrieved from `https://www.fdsn.org/networks/detail/NY/` (Seismic Network) doi: 10.7914/SN/NY

U.S. Geological Survey. (2016). *U.S. Geological Survey Networks* [data set]. International Federation of Digital Seismograph Networks. Retrieved from `https://www.fdsn.org/networks/detail/GM/` (Seismic Network) doi: 10.7914/SN/GM

VanDecar, J., & Crosson, R. (1990). Determination of teleseismic relative phase arrival times using multi-channel cross-correlation and least squares. *Bull. Seis. Soc. Am.*, *80*(1), 150-169.

Various Authors. (1965). *International Miscellaneous Stations (IMS)* [data set]. International Federation of Digital Seismograph Networks. Retrieved from `https://www.fdsn.org/networks/detail/IM/` (Seismic Network)

Woods Hole Oceanographic Institution (WHOI). (2010). *Cascadia- Keck* [data set].

International Federation of Digital Seismograph Networks. (Seismic Network)

Yukon Geological Survey. (206). *Yukon Observatory (YO)* [data set]. International Federation of Digital Seismograph Networks. Retrieved from `https://www.fdsn.org/networks/detail/YO_2016/` (Seismic Network)